

Polarization Entanglement Distribution in Ensemble-Based Atomic Memories

Bhaskar Mookerji*

Massachusetts Institute of Technology, Cambridge, Massachusetts 02139, USA

Jeffrey H. Shapiro†

Massachusetts Institute of Technology, Research Laboratory of Electronics, Cambridge, Massachusetts 02139, USA

(Dated: February 28, 2012)

Quantum networks enable the long-distance communication of quantum states through teleportation, but require, in advance, the robust distribution of entanglement between relevant parties. Engineering these networks requires quantum interconnects, which convert quantum states in one physical system to those of another reversibly, and with high fidelity. In the following, we describe implementations of long-distance quantum communication networks using polarization entanglement and atomic ensembles. We concisely describe the interactions of a quantum optical field with a heralding atomic ensemble, accounting for multiple-pair events at entanglement generation, as well as finite transmission and photodetection efficiencies under number-resolving and non-resolving photodetection schemes. Using these results, we perform a detailed quantitative performance analysis of quantum networks that distribute and swap entanglement.

I. INTRODUCTION

Quantum communication exploits quantum mechanical resources, such as entanglement, to achieve tasks unrealizable by classical means, such as accurate teleportation of quantum states and unconditionally secure private key distribution. For such applications, the fundamental problem of quantum communication is the establishment, over optical channels, of entanglement between distant nodes. However, the rate of entanglement distribution to nodes decreases exponentially with channel length. The possibility of creating *scalable* optical quantum networks requires that we overcome this difficulty by storing and processing quantum information locally in quantum memories: first, as repeaters increasing network scalability, and second, as light-matter interfaces to quantum computers [1].

We address the following open problem: the theoretical limits of atomic-ensemble quantum memories that store polarization entanglement and the system performance of ensemble-based hybrid systems in quantum communication. The overall approach marries the formalism of collective interactions of atomic ensembles and quantum optical fields with a number-state analysis of our architecture's performance. This analysis focuses on four areas. We first introduce pre-existing memory and repeater architectures forming the foundation of this work, and discusses the importance of polarization entanglement to quantum communication (Section I). We also summarize the atomic physics concerning the interactions between multi-atom ensembles and quantized light fields, particularly in the context of three-level Raman interactions. We abstract quantized light-ensemble interactions within a heralding atomic memory as a trilinear Hamiltonian

and determine that these interactions preclude a Gaussian state analysis of local entanglement distribution.

After describing the potential losses in an entanglement distribution architecture, we apply the $SU(2)$ representation of beam splitter operators to model loss in a number state basis, and perform a Gaussian state analysis of polarization entanglement swapping (Section II and III). A number-state analysis of the entanglement distribution captures the joint state of the heralding light and atomic excitations, accounting for imperfections in transmission loss, photodetection efficiency and counting resolution, and multiple-pair events at the entanglement source. This numerical characterization of entanglement distribution and connection presented here is so far consistent with our physical intuition of how such networks should behave. In particular, the probability of a successful heralding event is independent of whether a single, significant, uniform efficiency loss is located either before or after an ensemble memory, or during photodetection. With regards to the probability measuring a single photon, all losses are effectively the same. The same is not true for fidelity of entanglement distribution. A uniform transmission loss between the entanglement source and the ensembles will significantly reduce the likelihood that you've stored a polarization Bell state, but significant quantum efficiency losses at photodetection are less likely to diminish that fidelity. Increasing the pump power at the entanglement source increases the likelihood of multiple-pair events, increasing the heralding probability but making the fidelity more sensitive to transmission and photodetection efficiency losses. These results are true for both number-resolving and non-resolving photodetectors. For both entanglement distribution and connection, heralding probabilities for non-resolving detectors are higher, but the fidelities are significantly lower. Many of these same issues appear in entanglement swapping as well.

Section IV discusses possible future directions for studying architectures for quantum communication with

* mookerji@mit.edu

† jhs@mit.edu



FIG. 1. Components of a quantum repeater node in the MIT-NU architecture. (a) Parametric downconversion creates pairs of polarization-entangled photons, sending the idler photon to atom-trap 1 and the signal photon to atom-trap 2. Each trap contains a single ultra-cold rubidium atom cooled to its hyperfine ground state. In the energy level diagram, the AB-transition absorbs 795 nm photons, and the BD-transition is coherently driven, thereby enabling storage at D. (b) Polarization-entangled photon pairs generated by a pair of type-II optical parametric amplifiers (OPAs) and a polarizing beam splitter (PBS). The polarizations \hat{x} and \hat{y} are denoted by arrows and bullets, respectively. Figures taken from [2] and [3].

polarization entanglement, such as the formalization of our number-state analysis, the inclusion of spin decoherence in quantum memories, and experimental issues relevant to the realization of these systems (e.g., spectral bandwidth requirements of the entanglement source, optical depth and Raman interaction in neutral atomic gases).

I.1. Architectures for Long-Distance Quantum Networks

An illustration of a model quantum communication system is shown in Fig. 1, in the case of a single-trapped atom. Through type-II parametric downconversion, a post-selected maximally-entangled state can be produced of the form,

$$|\psi_1\rangle = \frac{1}{\sqrt{2}} (|\sigma_+\rangle_1 |\sigma_-\rangle_2 + e^{i\phi} |\sigma_-\rangle_1 |\sigma_+\rangle_2) \quad (1)$$

where σ_+ (σ_-) indicates right (left) circular polarization, and ϕ is a phase offset. An arbitrary polarization of any

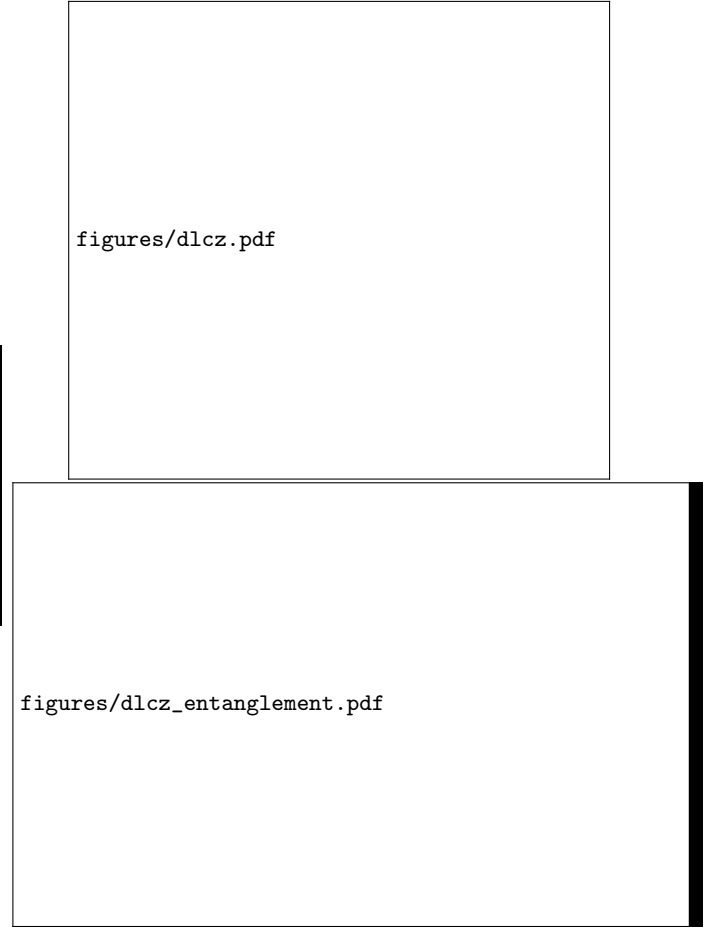


FIG. 2. Entanglement with the DLCZ protocol. (Left) Weak and strong coherent pulses induce writing and reading through spontaneous Raman transitions, respectively. (Right) Measurement-induced interference results in a single-excitation entangled state. Figures taken from [1] and [4].

photon entering the cavity can be stored in the basis of right and left circular polarizations, such that

$$|\psi_2\rangle = \alpha |\sigma_+\rangle + \beta |\sigma_-\rangle. \quad (2)$$

Through a Raman Λ -type interaction, a signal or idler photon effectively transfers its entanglement to the degenerate B magnetic hyperfine levels, and subsequently to the D levels through a coherently-driven transition. However, the efficient coupling of a single photon to a single trapped atom is a daunting technical task, requiring that the atom be held in an ultrahigh- Q cavity. By using an atomic ensemble, we eliminate the need for such a high-quality cavity because a collective atomic state is easily produced by a single photon. Such a state is one in which a single atom has been excited from its ground state $|g\rangle$ at A to the metastable state $|s\rangle$ at D.

To illustrate this behavior for an atomic ensemble, consider N_a atoms prepared in their ground states, a collective state denoted by $|0\rangle_a = |g\rangle^{\otimes N_a}$. Coherently pumping the ensemble creates an inelastic Raman scattering event

that is collectively enhanced by constructive interference within the ensemble [5]. The resulting forward-scattered Stokes light arises from coherent spontaneous emission in the ensemble, and the correlated ensemble excitation is a collective spin state,

$$|1\rangle_a = \hat{S}^\dagger |0\rangle_a = \frac{1}{\sqrt{N_a}} \sum_{i=1}^{N_a} |g\rangle_1 \cdots |s\rangle_i \cdots |g\rangle_{N_a}. \quad (3)$$

where $\hat{S} = (1/\sqrt{N_a}) \sum_i |g\rangle_i \langle s|$. Because the excitation is composed of many atoms, the collective spin excitation is protected against the loss of individual atoms in the ensemble, increasing its robustness for storage. In the weak interaction limit, in which most of the atoms remain in their ground state, the spin excitation \hat{S} is effectively a ladder operator, as $[\hat{S}, \hat{S}^\dagger] = \sum_i (|g\rangle_i \langle g| - |s\rangle_i \langle s|) / N_a \approx 1$, and the outgoing Stokes light and spin excitation are in a two-mode squeezed state [4]. Generally, the term with the n th atom in $|s\rangle$ acquires the phase $e^{i(\mathbf{k}_w - \mathbf{k}_s) \cdot \mathbf{x}_n}$, where \mathbf{k}_w is the wave vector of pump field, \mathbf{k}_s is that of the detected Stokes photon, and \mathbf{x}_n is the n th atom's position. Collective excitations can be read out very efficiently when converted into single anti-Stokes photons, which are emitted into a well-defined mode because of collective interference. A resonant laser excitation of the collective state in Eqn. 3 results in $N_a - 1$ atoms in $|g\rangle$ and one delocalized excitation in $|e\rangle$. Through decay to the $|g\rangle^{\otimes N_a}$, an anti-Stokes photon is emitted along the $|e\rangle - |g\rangle$ transition. Denoting \mathbf{k}_{as} and \mathbf{k}_r as the wave vectors of the anti-Stokes photon and read laser, respectively, satisfying the phase matching condition $\mathbf{k}_s + \mathbf{k}_{as} = \mathbf{k}_r + \mathbf{k}_w$ results in a very high probability amplitude for the anti-Stokes photon to be in the $\mathbf{k}_r + \mathbf{k}_w - \mathbf{k}_s$ direction due to constructive interference [6].

Our analysis merges the approaches of trapped single atoms in cavity quantum electrodynamics (QED) proposed by MIT and Northwestern University (MIT-NU) and the ensemble-based repeater architecture proposed by Duan, Lukin, Cirac, and Zoller (DLCZ) [2, 4]. The MIT-NU and DLCZ protocols both utilize spontaneous Raman transitions to mediate atomic storage. Whereas the MIT-NU protocol has the advantage of storing externally generated entanglement and verifying its success through cycling-transition fluorescence, it is prohibitively difficult to implement because of the strong coupling requirements of cavity QED.

In contrast, the DLCZ protocol creates a collective atomic excitation, as in Eqn. 3, not by an external input photon, but by the ensemble itself interacting with a classical (write) field. The entangled state is generated probabilistically (but heralded) through postselection and measurement quantum interference, as shown in Fig. 2. In the ideal case of low excitation probability, a photodetection event at either of the two detectors projects the two ensembles into a maximally-entangled singlet state of excitations. Although scalably resilient to issues that might plague such protocols, such as propagation loss and photodetector dark counts, DLCZ re-

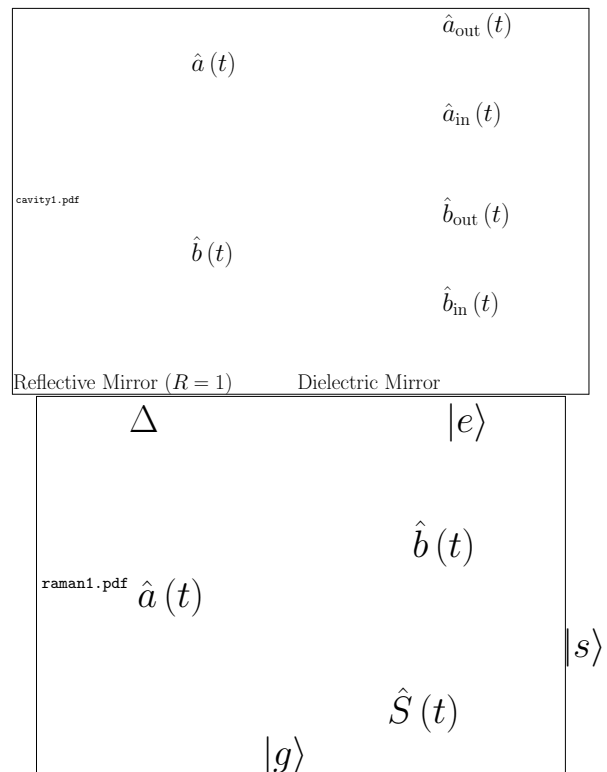


FIG. 3. DLCZ with quantum field inputs. (Left) Input-output formalism for a single-sided, two-mode ring cavity. (Right) Interaction in a three-mode parametric amplifier

quires stable phase coherence and number-resolving photodetectors, neither of which are easy to implement in practice. By enabling the storage of externally-generated entanglement in a DLCZ-type protocol, we will address new error models for entanglement fidelity in quantum memories.

We abstracted a model for the interaction of input quantum field into an ensemble-based quantum memory. A basis for this model is inspired by recent experimental work on heralded single-photon atomic memories and interfaces from [7] [6], which utilized two spatially-overlapping atomic ensembles to absorb arbitrarily polarized single photons. Heralding was observed (at rate of 10^{-6} , using pulsed coherent states ($\bar{N} \approx 500$) with an absorption probability $\alpha = 0.01$). Despite operating in an effective single-photon regime, multiple photon inputs were still present, a problem we wish to analyze in the case of a parametric downconverter input. We consider an ensemble of Λ -type atoms confined in a single-sided, low-finesse ring cavity, as shown in Fig. 3. The $|g\rangle - |e\rangle$ and $|e\rangle - |s\rangle$ transitions are coupled to the cavity modes \hat{a} and \hat{b} , respectively, each with coupling coefficient g_c . Under the rotating wave approximation, the interaction Hamiltonian for the collective interaction process is given by

$$\hat{H} = \hbar\Gamma (\hat{a}\hat{S}^\dagger\hat{b}^\dagger + \hat{b}\hat{S}\hat{a}^\dagger) \quad (4)$$

where $\Gamma = g_c^2 N_a / \Delta$ (Δ is the detuning from the two-photon resonance). In general, a Hamiltonian that cannot be analytically diagonalized will not have analytical dynamics [8, 9], and will therefore not be useful in a Gaussian state analysis. A three-mode interaction describes a heralding quantum memory where an input quantum field (pump mode \hat{a}) creates a stationary ensemble excitation (idler mode \hat{b}) and a heralding Stokes photon (signal mode \hat{S}). Parameterizing the strength of this interaction by Γ , the trilinear Hamiltonian describing this process is then

$$\hat{H} = \hat{H}_0 + \hat{H}_{\text{int}} \quad (5)$$

where

$$\hat{H}_0 = \omega_a \hat{a}^\dagger \hat{a} + \omega_b \hat{b}^\dagger \hat{b} + \omega_S \hat{S}^\dagger \hat{S} \quad (6)$$

$$\hat{H}_{\text{int}} = \Gamma \hat{a} \hat{b}^\dagger \hat{S}^\dagger + \Gamma^* \hat{S} \hat{b} \hat{a}^\dagger \quad (7)$$

with

$$[\hat{H}_0, \hat{H}_{\text{int}}] = 0. \quad (8)$$

assuming that each mode begins from rest, we can also say that

$$\hat{N}_{abc} = 2\hat{a}^\dagger \hat{a} + \hat{b}^\dagger \hat{b} + \hat{S}^\dagger \hat{S} \quad \hat{N}_{bc} = \hat{b}^\dagger \hat{b} - \hat{S}^\dagger \hat{S} \quad (9)$$

are conserved quantities. In Section II, we assume an *ansatz* solution such that N entangled photons are absorbed by an ensemble memory and are converted, without loss, to N spin excitations and N heralding photons. Note that that operations preserving the Gaussian properties of a quantum state's Wigner function (e.g., for polarization-entangled light) must be quadratic in its boson operator terms [10]. Any quadratic interaction Hamiltonian is thus a Gaussian operation, and the solutions for its input-output behavior is a Bogoliubov transformation of the input modes. However, it is not even possible to determine the analytical dynamics for Eqn. 7, because it is not a quadratic Hamiltonian. In the following section, we will describe some subtleties and prospects for achieving strong interactions between quantized excitations, in the trilinear case.

We can compensate for finite detunings and heralding probabilities in these ensembles by increasing the ensemble's optical depth, which is limited in free-space interactions by ensemble size and coupling strength. Several approaches use multi-pass optical cavities to increase the likelihood of a successful Raman scattering event between a cavity field and the enclosed ensemble [7, 11–14]. The cavity-ensemble heralding efficiency is captured by the cooperativity parameter $C = g_c^2 N_A / \kappa_c \gamma$, where g_c is the single-atom coupling constant to the cavity mode, κ_c is the cavity decay rate, and γ is the excited state spontaneous decay rate. It can be shown that the cooperativity is approximately $C \sim fd$, where d is the optical depth

of the ensemble and the finesse f is approximately the number of passes the optical field makes in the cavity. Optical cavities are used in the magnon-type memory, in which a single collective excitation is shared between two spatially-overlapping atomic ensembles [6]. Photons of arbitrary polarization states are stored between two ensembles that absorb only left- (σ^+) and right-circularly (σ^-) polarized light, respectively, and emit only linearly (π) polarized light into the cavity resonator, thereby eliminating any which-path information. The memory itself is an ensemble of approximately 8000 cesium atoms loaded from a far-detuned magneto optical trap (MOT) into a one-dimensional optical lattice overlapping a medium-finesse ($f = 140$) optical cavity. A spatially homogenous, DC magnetic field allows time-dependent control of polarization storage through Larmor precession of the ensembles magnetic moment. In theory, single-photon conversion efficiencies for this type of magnon memory are quite high.

As an aside, it is worth noting a competing approach to photon storage that may serve as a useful comparison in the future, namely, the usage of stimulated Raman transitions and electromagnetically induced transparency (EIT) to increase the coupling of an input quantum field with an atomic ensemble [15–18]. In this approach, an external coherent control field couples the $|e\rangle - |s\rangle$ transition in a Λ -type atom, adiabatically reducing the group velocity of a single photon wavepacket and trapping it within the ensemble. Such an approach is deterministic, with high throughput, but admits neither easy verification (as in MIT-NU) nor heralding (as in DLCZ). Like the DLCZ protocol above, its compatibility with externally-generated entanglement is an open question.

I.2. Polarization Quantum Entanglement and Communication

Because we will be concerned with the behavior of atomic ensembles that are illuminated by the entangled signal and idler produced by optical parametric amplification (OPA), it is important to have an appropriate model for such light beams. As our goal is to quantify the effects of multiple-pair emissions from such a source on the resulting stored entanglement, we cannot immediately default to a postulated biphoton picture. Instead, we shall use the full Gaussian-state description, in which the the input field in this interaction is one of a pair of polarization-entangled light beams generated by the interference of a pair of anti-phased optical parametric amplifiers as shown in Fig. 1. We assume that the signal and idler cavities are matched with identical linewidths Γ , and pumping fractions, G^2 , of oscillation threshold, with no depletion of or excess noise on the pump [3, 19]. Following interference, the output fields are in an entangled, zero-mean Gaussian pure state with the normally-

ordered and phase-sensitive correlation functions

$$\begin{aligned} \langle \hat{A}_{k_j}^\dagger(t+\tau) \hat{A}_{k_j}(t) \rangle &= \frac{G\Gamma}{2} \left[\frac{e^{-(1-G)\Gamma|\tau|}}{1-G} - \frac{e^{-(1+G)\Gamma|\tau|}}{1+G} \right] \\ \langle \hat{A}_{S_j}(t+\tau) \hat{A}_{I_j}(t) \rangle &= \frac{(-1)^{j-1} G\Gamma}{2} \left[\frac{e^{-(1-G)\Gamma|\tau|}}{1-G} + \frac{e^{-(1+G)\Gamma|\tau|}}{1+G} \right], \quad (10) \end{aligned}$$

where $\{\hat{A}_{k_j}(t) e^{-j\omega_k t} : k = S \text{ (signal)}, I \text{ (idler)}, j = 1, 2\}$ are the positive-frequency, photon-units OPA-output fields. The low-flux output state of this process at a detuning $\Delta\omega$ is given by expanding out the number ket representations of the OPAs to first order,

$$\begin{aligned} |\psi\rangle_{\text{SI}} &= \sum_n \sqrt{\frac{\bar{N}}{(\bar{N}+1)^{n+1}}} |n\rangle_{S_x} |n\rangle_{I_y} \\ &\quad \otimes \sum_n (-1)^n \sqrt{\frac{\bar{N}}{(\bar{N}+1)^{n+1}}} |n\rangle_{S_y} |n\rangle_{I_x} \\ &\approx |\text{vac}\rangle + \sqrt{\frac{\bar{N}}{(\bar{N}+1)^3}} (|H\rangle_S |V\rangle_I - |V\rangle_S |H\rangle_I), \quad (11) \end{aligned}$$

where $\bar{N} = 4G^2 / [(1-G^2 - \Delta\omega^2/\Gamma^2)^2 + 4\Delta\omega^2/\Gamma^2]$ is the average photon number per mode; and $|H\rangle_S = |1\rangle_{S_x} |0\rangle_{S_y}$, $|V\rangle_S = |0\rangle_{S_x} |1\rangle_{S_y}$, $|H\rangle_I = |1\rangle_{I_x} |0\rangle_{I_y}$, and $|V\rangle_I = |0\rangle_{I_x} |1\rangle_{I_y}$. Following measurement postselection, this state is a maximally entangled singlet state of the form in Eqn. 1 [19], and expansions to higher orders account for multiple-pair effects. A useful property of the full state $|\psi\rangle_{\text{SI}}$ is that its anti-normally ordered characteristic function is a zero-mean, jointly Gaussian distribution that remains Gaussian under linear transformations. Its joint density operator is $\hat{\rho}_{SI} = \hat{\rho}_{S_x I_y} \otimes \hat{\rho}_{S_y I_x}$, whose anti-normally ordered characteristic functions are given by

$$\begin{aligned} \chi_A^{\rho_{S_x I_y}}(\zeta_S, \zeta_I) &= \langle e^{-\zeta_S^* \hat{a}_{S_x} - \zeta_I^* \hat{a}_{I_y}} e^{\zeta_S \hat{a}_{S_x}^\dagger + \zeta_I \hat{a}_{I_y}^\dagger} \rangle \\ &= e^{-(1+\bar{N})(|\zeta_S|^2 + |\zeta_I|^2) + 2\bar{N}\text{Re}(\zeta_S \zeta_I)} \quad (12) \end{aligned}$$

and

$$\begin{aligned} \chi_A^{\rho_{S_y I_x}}(\zeta_S, \zeta_I) &= \langle e^{-\zeta_S^* \hat{a}_{S_y} - \zeta_I^* \hat{a}_{I_x}} e^{\zeta_S \hat{a}_{S_y}^\dagger + \zeta_I \hat{a}_{I_x}^\dagger} \rangle \\ &= e^{-(1+\bar{N})(|\zeta_S|^2 + |\zeta_I|^2) - 2\bar{N}\text{Re}(\zeta_S \zeta_I)}, \quad (13) \end{aligned}$$

which contain all multiple-pair orders of $|\psi\rangle_{\text{SI}}$. Following a linear transformation, the output state $\hat{\rho}_{\text{out}}$ can be determined by taking the inverse Fourier transform of the output characteristic function, with that characteristic function being easily calculated from the input characteristic function and the field transformation. In a memory or teleportation architecture, we want the output—represented by a pure or mixed state $\hat{\rho}_{\text{out}}$ —to have the highest possible fidelity with respect to its input

figures/connection.pdf

FIG. 4. Principle of a quantum repeater architecture. Entanglement is independently created at short distances between nodes AB...YZ. Entanglement is swapped between neighboring links such that locations A and D, for example, share entanglement over an intermediate distance. Swapping occurs over successively larger distances until links at the desired separation, A and Z, are entangled. Figure based on [20].

state $\hat{\rho}_{\text{in}}$. The trace separation quantifies this fidelity as $F(\hat{\rho}) = \text{Tr}[\sqrt{\hat{\rho}_{\text{out}} \hat{\rho}_{\text{in}} \sqrt{\hat{\rho}_{\text{out}}}}]$, which reduces to a projection overlap $\langle \psi_{\text{in}} | \hat{\rho}_{\text{out}} | \psi_{\text{in}} \rangle$ when the input is the pure state $\hat{\rho}_{\text{in}} = |\psi_{\text{in}}\rangle \langle \psi_{\text{in}}|$.

The most immediate problem affecting the distribution of polarization-entangled photons is photon propagation loss. Although a 1 km length of low-loss, optical telecom fiber ($\lambda = 1.55 \mu\text{m}$)—a relatively short distance—has a transmission nearing 95%, photon transmission decays exponentially with increasing distances, ruling out direct transmission of entangled photons over hundreds of kilometers. In classical communication, this type of signal attenuation is easily compensated with fiber-based amplifiers. However, for quantum communication, the no-cloning theorem prevents noiseless amplification of the non-orthogonal quantum states required for teleportation [21].

Fig. 4 shows a ‘quantum repeater’ approach that overcomes the amplifier restriction by incrementally extending entanglement across a larger network [20]. Lettered boxes represent memories, and pairs of memories form nodes on the network. For two nodes, A—B and C—D, that are each separately entangled, a joint Bell measurement between memories B and C will entangle systems A and D. This process, known as *entanglement swapping*, establishes entanglement between two networks links that may have never interacted. One can then establish entanglement between memories A and Z that are separated by a distance L by independently creating entanglement at N equally-spaced adjacent nodes out of $2N$ memories. $N - 1$ entanglement swapping operations in this network ultimately entangle memories A and Z. For the repeater protocol to work in an asynchronous fashion, these links must be heralding quantum memories. Together, entanglement repeaters and teleportation form basis for high-fidelity communications of quantum

states over long distances.

II. HERALDED POLARIZATION ENTANGLEMENT DISTRIBUTION WITH ATOMIC ENSEMBLES

This section combines the operating principles of ensemble-based quantum memories with architectures for polarization entanglement distribution, entanglement connection, and quantum teleportation. We will first discuss our architecture for entanglement distribution and provide a very basic abstraction for quantum memories. The remainder characterizes figures of merit—fidelity, heralding probability, and protocol success probability—under various transmission loss and photodetection conditions.

II.1. Architecture Overview and Figures of Merit

We will first discuss our overall architecture and loss model, followed by particular details of a dual-OPA polarization entanglement source and quantum memories. Our architecture for polarization entanglement distribution, shown in Fig. 5, is a modification of the standard DLCZ architecture shown in Fig. 2. In the original DLCZ protocol, both ensembles are coherently pumped and the probability that both ensembles will emit single photons is low compared to that for emission from a single ensemble. Interference at the 50-50 beam splitter in Fig. 2 erases any which-path information for the emission event, so a single detection at either photon counter D_1 or D_2 is used to herald entanglement of the two ensembles. The ideal situation in Fig. 5 is when a polarization singlet is emitted from the source and the overall system is lossless. The polarizing beam splitters (PBS) then load the signal and idler photons from the singlet into a coherent superposition of excitations of ensembles 1 and 2 and ensembles 3 and 4, respectively. This loading is heralded by the single-photon detections from pair (D_1, D_2) and (D_3, D_4) .

Fig. 6 encompasses the error modes for the Fig. 5 distribution architecture. The Type-II SPDC source may produce multiple signal-idler pairs, which will be modeled with the full joint Gaussian state description of its output. Propagation losses between the PBS and the atomic ensembles (labelled ‘pre’), and between the atomic ensembles and the 50-50 beam splitter (labelled ‘post’) are modeled by fictitious beam splitters whose vacuum-state input ports inject Gaussian quantum noise. Finite quantum efficiency photodetectors (labelled ‘pho’)

are similarly modeled, and we have ignored dark counts, which are known to be reasonably low at heralding wavelengths for silicon Geiger-mode avalanche photodiodes (APDs) [22]. Our number state model for these fictitious beam splitters, described in Section ??, includes the effects of phase differences between input ports, which we can use to characterize the effects of phase mismatch between pairs of ensembles. We will assume that any accumulated phase offsets leading to the ensembles can be incorporated into the pre-transmission efficiency.

The preceding imperfections expose two fundamentally different failure modes for this protocol that affect fidelity and probability of success, respectively. First, is it possible for heralding detections at the APDs to declare the protocol’s success even when the ensembles themselves are not in a polarization singlet state. For example, a multiple-pair event from the entanglement source could lead to multiple heralding photons emitted by a quantum memory. Post-memory attenuation and finite-quantum efficiency photodetection could eliminate all but one of those heralding photons, and the usage of Geiger-mode APDs might completely preclude our ability to distinguish between multiple-photon and single-photon events. A relative phase offset between two ensembles, either because of pump photon phase mismatch or pre-transmission phase accumulation, would similarly affect the final fidelity of the loaded quantum state. Lastly, because post-memory imperfections reduce potential heralding detections, it is possible to declare the protocol a failure—and reduce the probability of success—even when the ensembles are successfully loaded.

We characterize this architecture’s performance of heralding entanglement distribution by determining its fidelity figure-of-merit and measurement statistics under different photodetection schemes: photon-number resolving detection (PNRD), which can distinguish between single-photon and multi-photon photodetection events; and non-resolving single-photon detection (NRPD), which is unable to exclude multi-photon error events. For these two schemes, the projective measurement operators \hat{M}_j ($j = 1, 2, 3, 4$) represent four successful heralding outcomes at the photodetectors D_i ($i = 1, 2, 3, 4$). The input to each 50-50 beam splitter in Fig. 5 is a superposition state of linearly co-polarized heralding photons from the atomic memories, so we expect that successful entanglement distribution to yield single clicks at the signal and idler photodetector pairs. This DLCZ-like protocol for heralded polarization entanglement distribution therefore requires the occurrence of a single detection on either photodetectors D_1 or D_2 , as well as a *corresponding event* on either D_4 or D_3 . In the following, successful heralding is given by the projective measurements

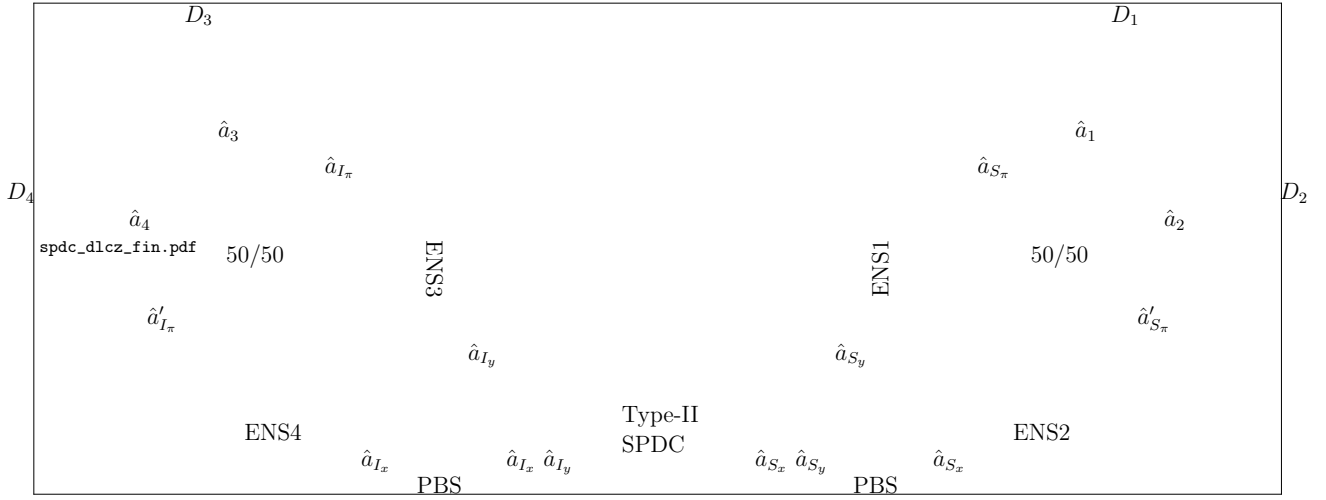


FIG. 5. Modified DLCZ architecture for distributing polarization entanglement, using a spontaneous parametric downconversion (SPDC) source and interferometer measurement for entanglement verification.

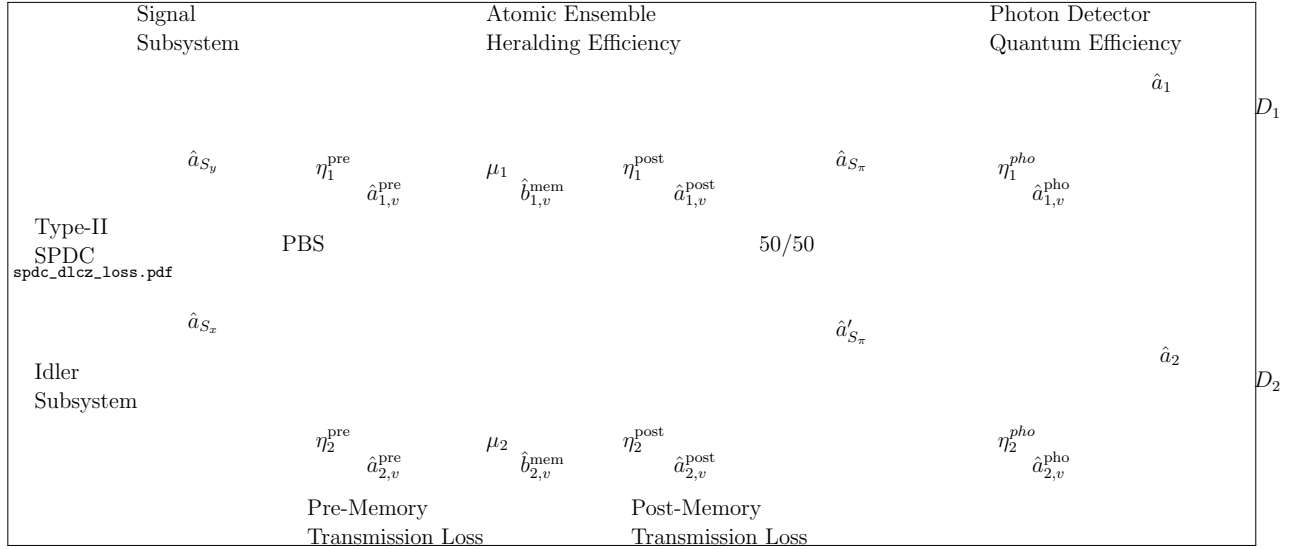


FIG. 6. Hong-Ou-Mandel (HOM) interferometer measurement with loss (labeled).

$$\hat{M}_j^{\text{PNRD}} = \begin{cases} (|1\rangle_{11} \langle 1|) \otimes (|0\rangle_{22} \langle 0|) \otimes (|1\rangle_{33} \langle 1|) \otimes (|0\rangle_{44} \langle 0|) & j = 1 \\ (|0\rangle_{11} \langle 0|) \otimes (|1\rangle_{22} \langle 1|) \otimes (|1\rangle_{33} \langle 1|) \otimes (|0\rangle_{44} \langle 0|) & j = 2 \\ (|0\rangle_{11} \langle 0|) \otimes (|1\rangle_{22} \langle 1|) \otimes (|0\rangle_{33} \langle 0|) \otimes (|1\rangle_{44} \langle 1|) & j = 3 \\ (|1\rangle_{11} \langle 1|) \otimes (|0\rangle_{22} \langle 0|) \otimes (|0\rangle_{33} \langle 0|) \otimes (|1\rangle_{44} \langle 1|) & j = 4 \end{cases}, \quad (14)$$

$$\hat{M}_j^{\text{NRPD}} = \begin{cases} (\hat{I}_1 - |0\rangle_{11} \langle 0|) \otimes (|0\rangle_{22} \langle 0|) \otimes (\hat{I}_3 - |0\rangle_{33} \langle 0|) \otimes (|0\rangle_{44} \langle 0|) & j = 1 \\ (|0\rangle_{11} \langle 0|) \otimes (\hat{I}_2 - |0\rangle_{22} \langle 0|) \otimes (\hat{I}_3 - |0\rangle_{33} \langle 0|) \otimes (|0\rangle_{44} \langle 0|) & j = 2 \\ (|0\rangle_{11} \langle 0|) \otimes (\hat{I}_2 - |0\rangle_{22} \langle 0|) \otimes (|0\rangle_{33} \langle 0|) \otimes (\hat{I}_4 - |0\rangle_{44} \langle 0|) & j = 3 \\ (\hat{I}_1 - |0\rangle_{11} \langle 0|) \otimes (|0\rangle_{22} \langle 0|) \otimes (|0\rangle_{33} \langle 0|) \otimes (\hat{I}_4 - |0\rangle_{44} \langle 0|) & j = 4 \end{cases}, \quad (15)$$

where $|n\rangle_i$ ($n = 0, 1$) are the vacuum and single-photon states, and \hat{I}_i is the identity operator for the \hat{a}_i mode

measured at photodetector D_i ($i = 1, 2, 3, 4$).

The heralding probability P_h is the probability a heralding—a (D_1, D_2) single click and a (D_3, D_4) single click. The success probability P_s is the probability that heralding has occurred and the four ensembles have loaded a polarization Bell state. The fidelity F_j is the projection of the post-heralding ensemble state onto the appropriate Bell state for \hat{M}_j heralding, i.e.,

$$\begin{aligned} & |\psi_j\rangle \\ &= \frac{1}{\sqrt{2}} \left(|1\rangle_S^1 |0\rangle_S^2 |0\rangle_S^3 |1\rangle_S^4 + (-1)^j |0\rangle_S^1 |1\rangle_S^2 |1\rangle_S^3 |0\rangle_S^4 \right) \\ & \quad (j = 1, 2, 3, 4). \end{aligned} \quad (16)$$

Following a photodetection measurement, the joint density operator of the four atomic ensembles is determined by applying \hat{M}_j and tracing over the optical modes:

$$\hat{\rho}_{\text{post}}^j = \frac{1}{P_j^h} \text{tr}_{1,2,3,4} \left(\hat{\rho}_{\text{out}} \hat{M}_j \right) \quad (17)$$

where $\hat{\rho}_{\text{out}}$ is the joint density operator of the heralding light fields and the ensembles

$$P_j^h = \text{tr} \left(\hat{\rho}_{\text{out}} \hat{M}_j \right). \quad (18)$$

If $|\psi_j\rangle$ is the entangled state of the four ensembles as heralded by \hat{M}_j , and the entanglement storage fidelity is F_j , we find that the success probability is

$$P_s = \sum_{j=1}^4 P_j^h F_j = \sum_{j=1}^4 \text{tr} \left(\hat{\rho}_{\text{out}} \hat{M}_j \right) \langle \psi_j | \hat{\rho}_{\text{post}}^j | \psi_j \rangle. \quad (19)$$

We will determine these measurement statistics using a full number-state analysis. Because the successful heralding outcomes defined by \hat{M}_j are symmetric, all the fidelities F_j are equal to each other. We will, therefore, calculate only F_1 without any loss of generality. In what immediately follows, we will formalize our approach for calculating the joint density operator of the light-ensemble system following entanglement distribution.

II.2. Photon Number Probability Distributions

Our first task is to concisely represent the effects of propagation loss on light beams of arbitrary statistical composition, as shown by the unitary beam splitter transformation in Fig. 7. The matrix representation of linear-loss beam splitters in Fig. 6 corresponds to the $\text{SU}(2)$ Lie group representation from angular momentum quantization [23]. We can use this equivalence to concisely relate the input and output field density operators from the loss using a joint photon-number probability distribution.

A two-port beam splitter with quantum efficiency η and input-field phase shifts ϕ_t and ϕ_r is described by the

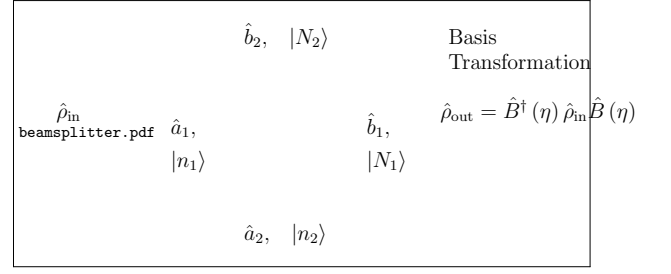


FIG. 7. Beam splitter action on an input density operator $\hat{\rho}_{\text{in}}$ with two input ports and two output ports. Labeled at each port are the input and output bases used in Eqns. 23 and 24. The boson annihilation operations at the input and output are \hat{a}_i and \hat{b}_i , respectively, and the accompanying index i represents signal ($i = 1$) and auxiliary modes ($i = 2$).

general $\text{SU}(2)$ beam splitter operator,

$$\hat{B}(\eta, \phi_t, \phi_r) = e^{-i(\phi_t - \phi_r)\hat{L}_3} e^{-2i \cos^{-1}(\sqrt{\eta})\hat{L}_2} e^{-i(\phi_t + \phi_r)\hat{L}_3}, \quad (20)$$

where the $\{\hat{L}_i\}$ are the Schwinger angular momentum operators for a two-dimensional quantum harmonic oscillator:

$$\begin{aligned} \hat{L}_1 &= \frac{1}{2} (\hat{a}_1^\dagger \hat{a}_2 + \hat{a}_2^\dagger \hat{a}_1) & \hat{L}_2 &= \frac{1}{2i} (\hat{a}_1^\dagger \hat{a}_2 - \hat{a}_2^\dagger \hat{a}_1) \\ \hat{L}_3 &= \frac{1}{2} (\hat{a}_1^\dagger \hat{a}_1 + \hat{a}_2^\dagger \hat{a}_2). \end{aligned} \quad (21)$$

Given a joint input state—either a pure state $|\psi\rangle_{\text{in}}$, or a pure or mixed state $\hat{\rho}_{\text{in}}$ —of the signal and auxiliary inputs, the output state of the beam splitter is

$$\hat{\rho}_{\text{out}} = \hat{B}^\dagger(\eta, \phi_t, \phi_r) \hat{\rho}_{\text{in}} \hat{B}(\eta, \phi_t, \phi_r). \quad (22)$$

In the number-state representation, as shown in Fig. 7, the beam splitter output of a general joint input state

$$\hat{\rho}_{\text{in}} = \sum_{n_1, n_2=0}^{\infty} \sum_{n'_1, n'_2=0}^{\infty} \rho_{\text{in}}(n_1, n_2; n'_1, n'_2) |n_1, n_2\rangle \langle n'_1, n'_2| \quad (23)$$

is,

$$\begin{aligned} \hat{\rho}_{\text{out}} &= \sum_{N_1, N_2=0}^{\infty} \sum_{N'_1, N'_2=0}^{\infty} \rho_{\text{out}}(N_1, N_2; N'_1, N'_2) \\ &\quad \cdot |N_1, N_2\rangle \langle N'_1, N'_2|. \end{aligned} \quad (24)$$

The output state (Eqn. 24) follows from the input state (Eqn. 23) by first applying the unitary beam splitter transformation in Eqn. 20, and then inserting the identity operator in the $|N_1, N_2\rangle$ basis. The output matrix elements in Eqn. 24 are

$$\begin{aligned} & \rho_{\text{out}}(N_1, N_2; N'_1, N'_2) \\ &= \sum_{n_1, n_2=0}^{\infty} \sum_{n'_1, n'_2=0}^{\infty} B_{N_1, N_2}^{n_1, n_2}(\cdot) \left[B_{N'_1, N'_2}^{n'_1, n'_2}(\cdot) \right]^* \\ &\quad \cdot \rho_{\text{in}}(n_1, n_2; n'_1, n'_2), \end{aligned} \quad (25)$$

where

$$\begin{aligned} B_{N_1, N_2}^{n_1, n_2}(\eta, \phi_t, \phi_r) &= \langle N_1, N_2 | \hat{B}^\dagger(\eta, \phi_t, \phi_r) | n_1, n_2 \rangle \\ &= R_{N_1, N_2}^{n_1, n_2}(\eta) e^{i\phi_t(N_1 - n_2) + \phi_r(N_1 - n_1)}. \end{aligned} \quad (26)$$

The transformation amplitudes R can be calculated in terms of the Jacobi polynomials $P_n^{(\alpha, \beta)}(x)$ as

$$\begin{aligned} R_{N_1, N_2}^{n_1, n_2}(\eta) &= \sqrt{\frac{N_1! N_2!}{n_1! n_2!}} \eta^{N_1 - n_2} (1 - \eta)^{N_1 - n_1} \\ &\cdot P_{N_2}^{(N_1 - n_1, N_1 - n_2)}(2\eta - 1), \quad N_1 \geq n_1, n_2, \end{aligned} \quad (27)$$

where

$$\begin{aligned} P_n^{(\alpha, \beta)}(x) &= \frac{(-1)^n}{2^n n!} (1 - x)^{-\alpha} (1 + x)^{-\beta} \\ &\cdot \left(\frac{d}{dx} \right)^n \left[(1 - x)^{n+\alpha} (1 + x)^{n+\beta} \right], \\ &\alpha, \beta > -1, \quad -1 \leq x \leq 1. \end{aligned} \quad (28)$$

The restriction $N_1 \geq n_1, n_2$ ensures the orthogonality of the Jacobi polynomials in Eqn. 27 over the range of quantum efficiency $0 \leq \eta \leq 1$; we will extend the range of this coefficient shortly. The R coefficient characterizes the output photon-number probability distribution for the joint input state $|n_1, n_2\rangle$. For a number-diagonal joint input state, it can be shown that

$$\begin{aligned} P_{\text{out}}(N_1, N_2) &= \langle N_1, N_2 | \hat{\rho}_{\text{out}} | N_1, N_2 \rangle \\ &= \sum_{\substack{n_1=0 \\ n_2=N_1+N_2-n_1}}^{N_1+N_2} P_{\text{out}}(N_1, N_2 | n_1, n_2) P_{\text{in}}(n_1, n_2), \end{aligned} \quad (29)$$

where the conditional and joint probabilities are

$$\begin{aligned} P_{\text{out}}(N_1, N_2 | n_1, n_2) &= \left[R_{N_1, N_2}^{n_1, n_2}(\eta) \right]^2 \\ P_{\text{in}}(n_1, n_2) &= \rho_{\text{in}}(n_1, n_2; n_1, n_2), \end{aligned} \quad (30)$$

respectively.

The beam splitter's physical symmetries allow us to extend the Jacobi polynomials over the full range photon-number output probabilities:

$$R_{N_1, N_2}^{n_1, n_2}(\eta) = \begin{cases} (-1)^{N_1 - n_1} R_{n_1, n_2}^{N_1, N_2}(\eta) & n_2 \leq N_1 < n_1 \\ R_{n_2, n_1}^{N_2, N_1}(\eta) & n_1 \leq N_1 < n_2 \\ (-1)^{N_1 - n_1} R_{N_2, N_1}^{n_2, n_1}(\eta) & n_1 > N_1, n_2 > N_1 \\ 0 & n_1 + n_2 \neq N_1 + N_2 \end{cases}. \quad (31)$$

We have made the unitary constraint explicit, as the Jacobi polynomials are not *ad hoc* restricted to events for which $n_1 + n_2 = N_1 + N_2$. Eqn. 25 simplifies because beam splitter unitarity requires $n_1 + n_2 = N_1 + N_2$ and $n'_1 + n'_2 = N'_1 + N'_2$. We thus eliminate the second and fourth summations in Eqn. 25 because $n_2 = N_1 + N_2 - n_1$ and $n'_2 = N'_1 + N'_2 - n'_1$, and restrict the remaining first and third summation there to $n_1 \in \{0, 1, \dots, N_1 + N_2\}$ and $n'_1 \in \{0, 1, \dots, N'_1 + N'_2\}$, respectively.

II.3. Calculation Examples — Lossless Case

Accounting for each linear loss and interference element described in Figures 5 and 6, we calculate the singlet-distribution fidelity and the protocol's probability of success by applying compositions of the beam splitter transformation described in Eqn. 22 to the Gaussian input state whose low-flux approximations becomes the singlet state in Eqn. 11. Together, Eqns. 25 and 27 abstract the the beam splitter's action, in the number-state basis, into a numerical calculation. Before analyzing the full architecture with all losses, we'll discuss two simpler

calculations—lossless distribution and distribution with pre-transmission and photodetection losses—that form the repertoire of techniques necessary for analysis of the general problems of interest.

Is the preceding mathematical formalism consistent with our expectations for lossless entanglement distribution? We assume that the input field phase shifts (ϕ_t, ϕ_r) are identically zero. Each of the four orthogonal signal and idler modes experience linear loss independently. Therefore, to avoid redundancy in the notation, we write the Gaussian state in Eqn. 11, at all orders, as

$$\begin{aligned} |\psi\rangle_{\text{in}} &= \sum_{n, m=0}^{\infty} (-1)^n \sqrt{\frac{\bar{N}^{n+m}}{(1 + \bar{N})^{n+m+2}}} \\ &\cdot |n\rangle_{S_y} |m\rangle_{S_x} |m\rangle_{I_y} |n\rangle_{I_x} \\ &\rightarrow \sum_{n, m=0}^{\infty} f_{n, m}(\bar{N}) |n_i\rangle^i, \end{aligned} \quad (32)$$

where $f_{n, m}(\bar{N})$ abstracts the thermal statistics of the OPAs. Any state or term having a variable indexed by i ($i = 1, 2, 3, 4$) actually denotes a product of four terms

acting at separately on those photodetection branches, similar to Einstein index notation, so that $|n_i\rangle^i \equiv |n\rangle_{S_y} |m\rangle_{S_x} |n\rangle_{I_y} |n\rangle_{I_x}$ and any usage of the n_i will have an implicit dependence on n and m . The complete conversion of a pump field by a quantum memory is then given by $|N_i^a\rangle_a |0\rangle_b^i |0\rangle_S^i \rightarrow |0\rangle_a^i |N_i^a\rangle_b^i |N_i^a\rangle_S^i$, where a , b , and S denote the pump, heralding, and spin excitation modes, respectively. All photons impinging on the ensembles that form the memory are converted into heralding photons and spin excitations. The resulting state of the heralding photons and the spin excitations in therefore

$$\begin{aligned} |\psi\rangle_{\text{post-ens.}} &= \sum_{n,m} (-1)^n \sqrt{\frac{\bar{N}^{n+m}}{(1+\bar{N})^{n+m+2}}} \\ &\quad \cdot |n\rangle_b^1 |m\rangle_b^2 |m\rangle_b^3 |n\rangle_b^4 |n\rangle_S^1 |m\rangle_S^2 |m\rangle_S^3 |n\rangle_S^4 \\ &\rightarrow \sum_{n,m} f_{n,m}(\bar{N}) |n_i\rangle_b^i |n_i\rangle_S^i. \end{aligned} \quad (33)$$

Following interference of the heralding photons at the beam splitters in Fig. 5, the joint state of the ensembles and the heralding photons at the photodetectors is

$$\begin{aligned} |\psi\rangle_{\text{out}} &= \sum_{N_i^p} \sum_{n,m} \underbrace{f_{n,m}(\bar{N})}_{\text{SPDC}} \underbrace{B_{N_2^p, N_1^p}^{n,m} \left(\frac{1}{2}\right) B_{N_4^p, N_3^p}^{m,n} \left(\frac{1}{2}\right)}_{\text{Interference Amplitude}} \\ &\quad \cdot |N_i^p\rangle_p^i |n_i\rangle_S^i, \end{aligned} \quad (34)$$

where we have suppressed the phase arguments in the beam splitter coefficients because $\phi_t = \phi_r = 0$. In Eqn. 34, the interference amplitude terms correspond to the mixing of m and n photons at both the signal and idler subsystems in Fig. 5, yielding N_i^p photons photons at the photodetector D_i . The joint output written as a pure-state density operator is thus

$$\begin{aligned} \hat{\rho}_{\text{out}} &= \sum_{N_i^p, N_i^{p'}} \sum_{n,m,n',m'} f_{n,m}(\bar{N}) f_{n',m'}(\bar{N}) B_{N_2^p, N_1^p}^{n,m} \left(\frac{1}{2}\right) \\ &\quad \cdot B_{N_4^p, N_3^p}^{m,n} \left(\frac{1}{2}\right) \left[B_{N_2^{p'}, N_1^{p'}}^{n',m'} \left(\frac{1}{2}\right) B_{N_4^{p'}, N_3^{p'}}^{m',n'} \left(\frac{1}{2}\right) \right]^* \\ &\quad \cdot |N_i^p\rangle_p^i |n_i\rangle_S^i \langle N_i^{p'}|_{p'}^i \langle n_i'|_S^i. \end{aligned} \quad (35)$$

anti Eqn. 18, we trace over all modes and find that photon number resolving detectors yield

$$\begin{aligned} P_1^h &= \sum_{n,m} \left| f_{n,m}(\bar{N}) B_{0,1}^{n,m} \left(\frac{1}{2}\right) B_{1,0}^{m,n} \left(\frac{1}{2}\right) \right|^2 \\ &= \frac{\bar{N}}{2(1+\bar{N})^3}, \end{aligned} \quad (36)$$

where the last equality is calculated by summation expansion. Following projective measurement, the joint

state of the ensembles is given by the mixed-state density operator,

$$\begin{aligned} \hat{\rho}_{\text{post}}^1 &= \frac{1}{P_1^h} \sum_{n,m,n',m'} f_{n,m}(\bar{N}) f_{n',m'}(\bar{N}) B_{0,1}^{n,m} \left(\frac{1}{2}\right) \\ &\quad \cdot B_{1,0}^{m,n} \left(\frac{1}{2}\right) \left[B_{0,1}^{n',m'} \left(\frac{1}{2}\right) B_{1,0}^{m',n'} \left(\frac{1}{2}\right) \right]^* |n_i\rangle_S^i \langle n_i'|_S^i, \end{aligned} \quad (37)$$

which, projected against the ideal singlet state $|\psi_1\rangle$ gives the fidelity of the entanglement distribution

$$\begin{aligned} F_1 &= \langle \psi_1 | \hat{\rho}_{\text{post}}^1 | \psi_1 \rangle \\ &= \frac{1}{2P_1^h} \sum_{n,m,n',m'} f_{n,m}(\bar{N}) f_{n',m'}(\bar{N}) B_{0,1}^{n,m} \left(\frac{1}{2}\right) B_{1,0}^{m,n} \left(\frac{1}{2}\right) \\ &\quad \cdot \left[B_{0,1}^{n',m'} \left(\frac{1}{2}\right) B_{1,0}^{m',n'} \left(\frac{1}{2}\right) \right]^* (\delta_{n,1} \delta_{m,0} - \delta_{n,0} \delta_{m,1}) \\ &= \frac{\bar{N}}{2P_1^h (1+\bar{N})^3} = 1, \end{aligned} \quad (38)$$

Here, the second and third terms from expanding the Kronecker delta expression cancel, and the last equality follows from Eqn. 36. Unity fidelity is the expected result in this ideal, lossless case. Because the post-measurement state is symmetric with respect to all \hat{M}_j , the protocol's overall success probability—defined by Eqn. 19—is four times the value we found in Eqn. 36,

$$P_s = \frac{2\bar{N}}{(1+\bar{N})^3}, \quad (39)$$

which equals the probability of successful generation of a single pair of signal and idler photons from a dual OPA source. Again, this is an expected result for the ideal case of lossless operation.

The non-resolving photodetection calculations are a bit more complicated, and there we use the identity

$$\text{tr}[|n\rangle \langle n'| (I - |0\rangle \langle 0|)] = 1 - \delta_{n,0} \delta_{n',0} \quad (40)$$

and the prior definition of a NRPD POVM measurement given in Eqn. 15. Applied to the joint state density operator in Eqn. 35, the post-measurement state of the ensembles is

$$\begin{aligned} \hat{\rho}_{\text{post}}^1 &= \sum_{n,m} \left| f_{n,m}(\bar{N}) B_{0,n+m}^{n,m} \left(\frac{1}{2}\right) B_{n+m,0}^{m,n} \left(\frac{1}{2}\right) \right|^2 |n_i\rangle_S^i \langle n_i|_S^i \\ &\quad (41) \end{aligned}$$

In the last step's simplification, we have enforced the photon number conservation constraint implicit in the definition of the beam splitter coefficient. For the sake of brevity, the details of the corresponding fidelity, heralding probability, and success probability calculations are

figures/nrpd_lossless_herald.pdf

figures/nrpd_lossless_fid.pdf

figures/nrpd_lossless_success.pdf

FIG. 8. Figures of merit for lossless architecture (PNRD and NRPD). Figures 8(a) and 8(b) show divergences between heralding probability and fidelity for PNRD (gray) and NRPD (black) architectures. The protocol’s overall success probability is identical in either case (Fig. 8(c)).

omitted, being straightforward extensions of PNRD calculation. Fig. 8 shows the combined results of the PNRD and NRPD calculations.

Despite the absence of losses in this example, we can still gain some intuition for the effects of different photodetection schemes on our figures of merit. Fig. 8 compares the resulting figures of merit between the PNRD and NRPD photodetection schemes in a lossless architecture in which increasing \bar{N} leads to an increasing likelihood of multi-pair emissions from the entanglement source. The heralding probability for the NRPD exceeds that for PNRD, which is not surprising, as PNRD forms a subset of the possible detection events present with the NRPD scheme. In the absence of loss, the NRPD fidelity is independent of detection events at either D_1/D_4 or D_2/D_3 and falls dramatically for high values of \bar{N} , being ultimately unable to distinguish between valid single-photon heralding events and higher-order excitations stored in the ensemble. The PNRD fidelity, on the other hand, holds at unity, because this detector perfectly identifies single-pair loading in the lossless scenario under consideration here. The success probability, however, is identical for the PNRD and NRPD schemes, because any decline in NRPD fidelity is compensated for by a corresponding increase in heralding probability. A single term in the success probability sum—the product of the fidelity and heralding probability—represents the joint probability of loading the required Bell state and the measurement of the corresponding heralding event. Single photon events do not require photon-number resolving capabilities, and as such, the loading success is equally likely under either scheme, when the system is lossless.

II.4. Calculation Examples — Pre-Transmission and Photodetection Losses

Including loss in our analysis introduces nested binomial distributions of pump and signal photons, and the added computational complexity of deeper and deeper nested summations. As such, the results of this example and all subsequent sections are calculated numerically, with a range of \bar{N} chosen so that the input Gaussian state can be safely truncated to a finite number of excitations. For all subsequent calculations in this thesis, \bar{N} ranges from 0.05 to 0.3 in steps of $\Delta\bar{N} = 0.05$, and we take $n_{\max} = m_{\max} = 3$ to be the maximum number of excitations. For the the full range of a single transmission efficiency $0 \leq \eta \leq 1$, it can be shown (numerically) that figures of merit, such as heralding probability, with higher truncation values differ insignificantly from those calculated at $n_{\max} = m_{\max} = 3$.

Introducing auxiliary vacuum states indexed by N^{pre} and N^{pho} , the joint output state of the heralded photons, ensemble excitations, and noise modes is given by,

$$|\psi\rangle_{\text{out}} = \sum_{N_i^a, N_i^{\text{pre}}, N_i, N_i^{\text{pho}}} \sum_{n,m} f_{n,m}(\bar{N}) B_{N_i^a, N_i^{\text{pre}}}^{n_i, 0}(\eta_i^{\text{pre}}) B_{N_2, N_1}^{N_1^a, N_2^a} \left(\frac{1}{2}\right) B_{N_4, N_3}^{N_3^a, N_4^a} \left(\frac{1}{2}\right) B_{N_i^p, N_i^{\text{pho}}}^{N_i, 0}(\eta_i^{\text{pho}}) |N_i^p\rangle_p^i |N_i^a\rangle_S^i |N_i^{\text{pre}}\rangle_{\text{pre}}^i |N_i^{\text{pho}}\rangle_{\text{pho}}^i \quad (42)$$

Eqn. 42 contains several important features. First, recall that each term indexed by i actually represents four independent terms. The n_i photons from the SPDC source mix with vacuum (zero photons), converting into N_i^a pump photons for the quantum memory and N_i^{pre} noise photons. The pump photons are completely converted into N_i^a heralding photons and N_i^a spin excitations. At the 50-50 beam splitter, the (N_1^a, N_2^a) and (N_3^a, N_4^a) photons interfere, yielding (N_1, N_2) and (N_3, N_4) photons which are each mixed with vacuum to yield N_i^p photons at each D_i photodetector. The summation lower limit for each summation variable is 0, and upper limit is given by the sum of the inputs to a given beam splitter (e.g., n_i for each the N_i^a and N_i^{pre} summations, $N_1^a + N_2^a$ for each of the N_1 and N_2 summations). Tracing out the noise modes and applying photon-number conservation to eliminate nested summations, the PNRD heralding probability for single-photon counts at detectors D_1 and D_4 is given by

$$P_1^{\text{PNRD}} = \left| f_{n,m}(\bar{N}) B_{N_i^a, n_i - N_i^a}^{n_i, 0}(\eta_i^{\text{pre}}) B_{N_2, N_1}^{N_1^a, N_2^a} \left(\frac{1}{2}\right) B_{N_4, N_3}^{N_3^a, N_4^a} \left(\frac{1}{2}\right) B_{1, N_1 - 1}^{N_1, 0}(\eta_1^{\text{pho}}) B_{0, N_2}^{N_2, 0}(\eta_2^{\text{pho}}) B_{0, N_3}^{N_3, 0}(\eta_3^{\text{pho}}) B_{1, N_4 - 1}^{N_4, 0}(\eta_4^{\text{pho}}) \right|^2. \quad (43)$$

From Eqn. 27, the photon-number probability amplitude following the OPA coefficient corresponds to the familiar binomial probability distribution that results from mixing of a number state with vacuum. Applying the NRPD POVM and photon-number conservation, as in Eqn. 37, and factoring the remaining photodetection efficiency amplitudes gives the heralding probability:

$$P_1^{\text{NRPD}} = \sum_{N_i^a, N_i} \sum_{n,m} \left| f_{n,m}(\bar{N}) B_{N_i^a, n_i - N_i^a}^{n_i, 0}(\eta_i^{\text{pre}}) B_{N_2, N_1}^{N_1^a, N_2^a} \left(\frac{1}{2}\right) B_{N_4, N_3}^{N_3^a, N_4^a} \left(\frac{1}{2}\right) B_{0, N_2}^{N_2, 0}(\eta_2^{\text{pho}}) B_{0, N_3}^{N_3, 0}(\eta_3^{\text{pho}}) \right|^2 \left[\left| B_{0, N_1}^{N_1, 0}(\eta_1^{\text{pho}}) \right|^2 - \sum_{N_1^p=0}^{N_1} \left| B_{N_1^p, N_1 - N_1^p}^{N_1, 0}(\eta_1^{\text{pho}}) \right|^2 \right] \left[\left| B_{0, N_4}^{N_4, 0}(\eta_4^{\text{pho}}) \right|^2 - \sum_{N_4^p=0}^{N_4} \left| B_{N_4^p, N_4 - N_4^p}^{N_4, 0}(\eta_4^{\text{pho}}) \right|^2 \right]. \quad (44)$$

The terms of this summation are also the diagonal coefficients of the ensembles' post-measurement density operator, which is required for calculating the fidelity and overall success probability of the protocol. To avoid redundancy, the numerical calculations of these quantities and their interpretation is described in Section II.5.

II.5. Full Loss Calculation (PNRD and NRPD)

In the previous section, we previewed a set of techniques used in the analysis of entanglement distribution, which we now use to account for all losses. In the following, we assume that the input field phase shifts (ϕ_t, ϕ_r) of each loss-modeling beam splitter are identically 0. As in the previous sections, we only list expressions for matching photodetection events at D_1 and D_4 , as corresponding expressions for D_2 and D_3 are given by simple substitution. Accounting for all losses, the full output state of the architecture, as shown in Fig. 6, is given by,

$$|\psi\rangle_{\text{out}} = \sum_{n,m} f_{n,m}(\bar{N}) \sum_{\substack{N_i^a, N_i^{\text{pre}}, N_i^l, N_i^{\text{post}}, \\ N_i, N_i^p, N_i^{\text{pho}}}} \left[\underbrace{B_{N_i^a, N_i^{\text{pre}}}^{n_i, 0}(\eta_i^{\text{pre}}) B_{N_i^l, N_i^{\text{post}}}^{N_i^a, 0}(\eta_i^{\text{post}})}_{\text{Pre-Interference Loss}} \underbrace{B_{N_2, N_1}^{N_1^l, N_2^l} \left(\frac{1}{2}\right) B_{N_4, N_3}^{N_3^l, N_4^l} \left(\frac{1}{2}\right)}_{\text{Interference Terms}} \underbrace{B_{N_i^p, N_i^{\text{pho}}}^{N_i, 0}(\eta_i^{\text{pho}})}_{\text{Photodetection Loss}} \right] \cdot \underbrace{|N_i^p\rangle_p^i |N_i^a\rangle_S^i}_{\text{Heralded \& Ensemble Modes}} \underbrace{|N_i^{\text{pho}}\rangle_{\text{pho}}^i |N_i^{\text{post}}\rangle_{\text{post}}^i |N_i^{\text{pre}}\rangle_{\text{pre}}^i}_{\text{Auxiliary Noise Modes}}. \quad (45)$$

and the corresponding joint density operator of the heralded photon and ensemble modes is

$$\begin{aligned} \hat{\rho}_{\text{out}}^{p,S} = & \sum_{\substack{n,m, \\ n',m'}} f_{n,m}(\bar{N}) f_{n',m'}(\bar{N}) \sum_{\substack{N_i^a, N_i^{\text{pre}} \\ N_i^{a'}, N_i^{\text{post}}}} \sum_{\substack{N_i^l, N_i^{\text{pre}} \\ N_i^{l'}, N_i^{\text{post}}}} B_{N_i^a, N_i^{\text{pre}}}^{n_i,0}(\eta_i^{\text{pre}}) B_{N_i^l, N_i^{\text{post}}}^{N_i^a,0}(\eta_i^{\text{post}}) \left[B_{N_i^{a'}, N_i^{\text{pre}}}^{n_i',0}(\eta_i^{\text{pre}}) B_{N_i^{l'}, N_i^{\text{post}}}^{N_i^{a'},0}(\eta_i^{\text{post}}) \right]^* \\ & \cdot \sum_{\substack{N_1, N_2, N_3, N_4 \\ N_1', N_2', N_3', N_4'}} B_{N_2, N_1}^{N_1', N_2'} \left(\frac{1}{2} \right) B_{N_4, N_3}^{N_3', N_4'} \left(\frac{1}{2} \right) \left[B_{N_2', N_1'}^{N_1', N_2'} \left(\frac{1}{2} \right) B_{N_4', N_3'}^{N_3', N_4'} \left(\frac{1}{2} \right) \right]^* \\ & \cdot \sum_{\substack{N_i^p, N_i^{\text{pho}} \\ N_i^{p'}, N_i^{\text{pho}'}}} B_{N_i^p, N_i^{\text{pho}}}^{N_i,0}(\eta_i^{\text{pho}}) \left[B_{N_i^{p'}, N_i^{\text{pho}'}}^{N_i',0}(\eta_i^{\text{pho}}) \right]^* |N_i^p\rangle_p^i |N_i^{a'}\rangle_S^i \langle N_i^{p'}|_p^i \langle N_i^{a'}|_S^i, \end{aligned} \quad (46)$$

and the PNRD probability that a heralding event \hat{M}_1 has occurred is then

$$\begin{aligned} P_1 = & \sum_{n,m} [f_{n,m}(\bar{N})]^2 \sum_{\substack{N_i^a, N_i^l \\ N_1, N_2, \\ N_3, N_4}} \left| B_{N_i^a, n_i - N_i^l}^{n_i,0}(\eta_i^{\text{pre}}) B_{N_i^l, N_i^a - N_i^l}^{N_i^a,0}(\eta_i^{\text{post}}) B_{N_2, N_1}^{N_1', N_2'} \left(\frac{1}{2} \right) B_{N_4, N_3}^{N_3', N_4'} \left(\frac{1}{2} \right) \right. \\ & \cdot B_{N_1, N_1-1}^{N_1,0}(\eta_1^{\text{pho}}) B_{N_2, N_2}^{N_2,0}(\eta_2^{\text{pho}}) B_{N_3, N_3}^{N_3,0}(\eta_3^{\text{pho}}) B_{N_4, N_4-1}^{N_4,0}(\eta_4^{\text{pho}}) \left. \right|^2. \end{aligned} \quad (47)$$

The results of numerical calculations with these expressions are shown in Figures 10 and 9. These figures distinguish between what we term ‘uniform’ and ‘non-uniform’ losses. Fig. 10 assumes that varying pre-transmission and photodetection losses are *identical* for all four arms of the interferometer, whereas Fig. 9 makes no such assumption by considering the effects of only a *single* loss or *paired* losses as labelled in the captions. The presence of uniform losses in one location—before or after the ensembles or during photodetections—has identical effects on the heralding probability. This heralding probability doesn’t depend on where a single uniform loss is located, as a pump photon lost prior to the ensemble or a heralding photon lost after the ensemble ultimately will have the same heralding result. This is definitely not the case for the F_1 fidelity, as a pre-transmission loss of a pump photon precludes successful entanglement distribution. In this case, it is difficult to tell if matching signal and idler photons were stored simultaneously. By contrast, any post-transmission or photodetection loss has a much smaller effect on the fidelity. Post-transmission and photodetection loss are quantitatively equal in their fidelity effects. Lastly, increasing pump power in the OPA source matches intuition, as increasing \bar{N} makes heralding events more likely, but decreases the desired fidelity due to multiple-pair effects.

In Fig. 9, we see that fidelity of entanglement is fairly robust against a single pre-transmission loss, as well as uniform losses present only in the signal subsystem or uniform losses between paths matched for a successful heralding event detection. Uniform losses shared between mis-matched paths (e.g., varying η_1 and η_3) degrade fidelity significantly, almost as though transmission loss were uniformly shared by all the paths as in Fig. 10(b).

The remaining analysis case is non-resolving photodetection (NRPD), which we show in Fig. 11. The details of this calculation are nearly identical to that shown in Sections II.3 and II.4. Not surprisingly, as in the lossless NRPD analysis, the heralding probability is higher than in the PNRD case, and increasing \bar{N} severely diminishes fidelity when both pre-transmission and photodetection losses occur. In the case of the latter, photodetection loss has almost no effect on the final fidelity of entanglement distribution. Pre-transmission losses in Fig. 11(a) demonstrate a residual dependence on pre-transmission loss for higher transmission efficiencies, consistent with our prior PNRD analysis.

III. ENTANGLEMENT CONNECTION

After successfully distributing entanglement to a pair of nodes, resulting in local entanglement, we will want to extend our quantum communication capabilities over distances prohibited by direct transmission. In this section, we use post-selected, polarization-entangled ensembles to accomplish a basic task in long-distance quantum communication, namely entanglement swapping. The high level concepts underlying this procedure was described in Section I.2 of this thesis’ introduction, and is a modification of the DLCZ protocol’s application to quantum communication [4].

Fig. 12 outlines a procedure for accomplishing polarization entanglement connection with atomic ensembles. Polarization entanglement is generated independently, at two different nodes, as described in Section II.1 and Fig. 4. A Bell-state measurement between the (S_y^A, S_x^A) and (S_y^B, S_x^B) ensemble pairs establishes polarization en-



FIG. 9. F_1 fidelities with non-uniform pre-transmission losses (PNRD) for $\bar{N} = 0.05 - 0.3$ ($\Delta\bar{N} = 0.05$). The caption in each subfigure specifies which of η_i^{pre} ($i = 1, 2, 3, 4$) is varied for that calculation; those not specified are fixed at 0.9.

tanglement between the remaining idler ensemble pairs (I_y^A, I_x^A) and (I_y^B, I_x^B) . Coherent, on-resonance pulses at each of the signal ensembles reads a Dicke excitation out of the $|s\rangle - |e\rangle$ atomic transition into a well-defined spatial mode. Loss-modeling beam splitters before interference (η_{pre}) and at photodetection (η_{pho}) characterize the quantum efficiency losses, although to maintain consistency with [24], we calculate fidelity with respect to $\eta_m = \eta_{\text{pre}}\eta_{\text{pho}}$. In the following, we determine the fidelity and probability of success when ensembles A and B are independently in singlet or Gaussian states.

Although a full Bell state measurement is not possible using linear optics [25], the observation of single clicks at both D_A and D_B , when these are unity quantum efficiency photon-number resolving detectors, uniquely heralds the measurement of a singlet state and successful completion of entanglement connection protocol when the A and B ensembles were both in their singlet states. Two signal ensemble pairs in independent singlet states

can be separated into four orthogonal basis states

$$\begin{aligned}
 |\psi\rangle^A \otimes |\psi\rangle^B &= \frac{1}{\sqrt{2}} (|H\rangle_{SA} |V\rangle_{IA} - |V\rangle_{SA} |H\rangle_{IA}) \\
 &\quad \otimes \frac{1}{\sqrt{2}} (|H\rangle_{SB} |V\rangle_{IB} - |V\rangle_{SB} |H\rangle_{IB}) \\
 &= |\phi_{yy}\rangle + |\phi_{yx}\rangle + |\phi_{xy}\rangle + |\phi_{xx}\rangle, \quad (48)
 \end{aligned}$$

where each $|\phi_{ij}\rangle$ ($i, j = x, y$) labels a joint state with signal-photon polarizations i and j in each path prior to interference. Because of photon-twinning at interference, only two of these orthogonal states— $|\phi_{xy}\rangle$ and $|\phi_{yx}\rangle$ —contribute to the probability of a heralding event: either (\hat{x}, \hat{y}) - or (\hat{y}, \hat{x}) -polarized photon pairs at (D_A, D_B) , with equal probability. As such, the entanglement connection fidelity will be unity in both the PNRD and the NPRD cases—

$$F_C = \frac{P_s}{P_h} = \frac{P_{xy} + P_{yx}}{P_{xy} + P_{yx}} = 1 \quad (49)$$

—independent of pre-transmission and photodetection quantum efficiency losses.

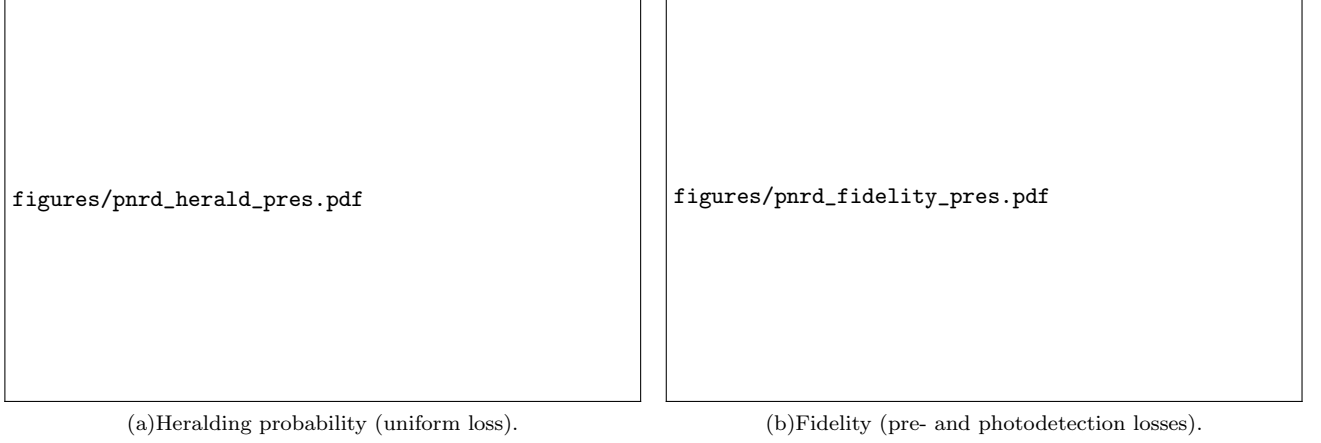


FIG. 10. Figures of merit with uniform losses (PNRD) for $\bar{N} = 0.05 - 0.3$ ($\Delta\bar{N} = 0.05$). Heralding probabilities are independent of a uniform loss' location: either before (pre-transmission) or after (post-transmission or photodetection) the ensemble (Fig. 10(a)). Pre-transmission losses preferentially decrease the fidelity of entanglement distribution compared to post-transmission and photo-detection losses (Fig. 10(b)).

Now let us consider performance when ensembles A and B are modeled as being in Gaussian states parameterized by an average spin excitation number \bar{N} . In the absence of any important nonlinear elements in Fig. 12, we will perform a characteristic function analysis instead of a number-state analysis. The joint density operator of these ensembles is $\hat{\rho}_{SI}^{\text{in}} = \hat{\rho}_{SI}^A \otimes \hat{\rho}_{SI}^B$, where $\hat{\rho}_{SI}^i = \hat{\rho}_{S_x^i I_y^i} \otimes \hat{\rho}_{S_y^i I_x^i}$ ($i = A, B$), which is represented by the anti-normally ordered characteristic function,

$$\begin{aligned} \chi_A^{\rho_{\text{in}}}(\zeta) &= \langle \prod_{i=A,B} D_A(\hat{a}_{S_y^i}, \zeta_{S_y^i}) D_A(\hat{a}_{S_x^i}, \zeta_{S_x^i}) \\ &\quad \cdot D_A(\hat{S}_{I_y^i}, \zeta_{I_y^i}) D_A(\hat{S}_{I_x^i}, \zeta_{I_x^i}) \rangle \\ &= \exp \left[- (1 + \bar{N}) \left(|\zeta_{S_y^A}|^2 + |\zeta_{S_x^A}|^2 + |\zeta_{I_y^A}|^2 + |\zeta_{I_x^A}|^2 \right) \right. \\ &\quad \left. - (1 + \bar{N}) \left(|\zeta_{S_y^B}|^2 + |\zeta_{S_x^B}|^2 + |\zeta_{I_y^B}|^2 + |\zeta_{I_x^B}|^2 \right) \right. \\ &\quad \left. + 2\text{Re} \left(\tilde{N} \zeta_{S_x^A} \zeta_{I_y^A} \right) - 2\text{Re} \left(\tilde{N} \zeta_{S_y^A} \zeta_{I_x^A} \right) \right. \\ &\quad \left. + 2\text{Re} \left(\tilde{N} \zeta_{S_x^B} \zeta_{I_y^B} \right) - 2\text{Re} \left(\tilde{N} \zeta_{S_y^B} \zeta_{I_x^B} \right) \right], \quad (50) \end{aligned}$$

where $\tilde{N} = \sqrt{\bar{N}(\bar{N} + 1)}$, $D_A(\hat{a}_i, \zeta_i) = e^{-\zeta_i^* \hat{a}_i} e^{\zeta_i \hat{a}_i^\dagger}$ is the antinormally-ordered displacement operator, and

$$\zeta = [\zeta_S, \zeta_I]^T = [\zeta_{S_y^A}, \zeta_{S_y^B}, \zeta_{S_x^A}, \zeta_{S_x^B}, \zeta_{I_y^A}, \zeta_{I_y^B}, \zeta_{I_x^A}, \zeta_{I_x^B}]^T. \quad (51)$$

The optical modes reaching the detectors D_i in Fig. 6 are

$$\begin{aligned} \hat{\mathbf{a}}_S^{\text{out}} &= \sqrt{\eta^{\text{pho}} \eta^{\text{pre}}} \mathbf{B} \hat{\mathbf{a}}_{\text{in}}^S + \sqrt{\eta^{\text{pho}} (1 - \eta^{\text{pre}})} \mathbf{B} \hat{\mathbf{a}}_v^{\text{pre}} \\ &\quad + \sqrt{1 - \eta^{\text{pho}}} \hat{\mathbf{a}}_v^{\text{pho}} \end{aligned} \quad (52)$$

where we have defined the operator-valued vectors

$$\begin{aligned} \hat{\mathbf{a}}_S^{\text{out}} &= [\hat{a}'_{S_y^A}, \hat{a}'_{S_y^B}, \hat{a}'_{S_x^A}, \hat{a}'_{S_x^B}]^T \\ \hat{\mathbf{a}}_S^{\text{in}} &= [\hat{a}_{S_y^A}, \hat{a}_{S_y^B}, \hat{a}_{S_x^A}, \hat{a}_{S_x^B}]^T \\ \hat{\mathbf{a}}^{\text{pre}} &= [\hat{a}_1^{\text{pre}}, \dots, \hat{a}_4^{\text{pre}}]^T \\ \hat{\mathbf{a}}^{\text{pho}} &= [\hat{a}_1^{\text{pho}}, \dots, \hat{a}_4^{\text{pho}}]^T \end{aligned} \quad (53)$$

with the linear transformation of the signal modes:

$$\mathbf{B} = \begin{bmatrix} \mathbf{M}_{2 \times 2} & \mathbf{0}_{2 \times 2} \\ \mathbf{0}_{2 \times 2} & \mathbf{M}_{2 \times 2} \end{bmatrix} \quad \mathbf{M}_{2 \times 2} = \frac{1}{\sqrt{2}} \begin{bmatrix} 1 & 1 \\ 1 & -1 \end{bmatrix}. \quad (54)$$

All of the idler modes $\hat{\mathbf{S}}_I^{\text{in}} = [\hat{S}_{I_y^A}, \hat{S}_{I_y^B}, \hat{S}_{I_x^A}, \hat{S}_{I_x^B}]^T$ remain unchanged. The Gaussian mixed-state of the Stokes light arriving at the detectors and the idler ensemble excitations is given by the antinormally-ordered characteristic function

$$\begin{aligned} \chi_A^{\rho_{\text{out}}}(\zeta, \tilde{\zeta}) &= \langle D_A(\hat{\mathbf{a}}_S^{\text{out}}, \zeta_S) D_A(\hat{\mathbf{S}}_I^{\text{in}}, \zeta_I) \rangle \\ &= \chi_A^{\rho_{\text{in}}} \left(\left[\sqrt{\eta_m} \tilde{\zeta}_{S_y^A}, \sqrt{\eta_m} \tilde{\zeta}_{S_y^B}, \sqrt{\eta_m} \tilde{\zeta}_{S_x^A}, \right. \right. \\ &\quad \left. \left. \sqrt{\eta_m} \tilde{\zeta}_{S_x^B}, \zeta_{I_y^A}, \zeta_{I_y^B}, \zeta_{I_x^A}, \zeta_{I_x^B} \right]^T \right) \\ &\quad \cdot e^{-\sum_{\{ \tilde{\zeta}_i \}} \eta^{\text{pho}} (1 - \eta^{\text{pre}}) |\tilde{\zeta}_i|^2 - \sum_{\{ \zeta_i \}} (1 - \eta^{\text{pho}}) |\zeta_i|^2} \end{aligned} \quad (55)$$

where the scaled $\tilde{\zeta}$ result from the transformation of the beam splitter transformation in Eqn. 54:

$$\tilde{\zeta} = \mathbf{B}^\dagger \zeta = \begin{bmatrix} \tilde{\zeta}_{S_y^A} \\ \tilde{\zeta}_{S_y^B} \\ \tilde{\zeta}_{S_x^A} \\ \tilde{\zeta}_{S_x^B} \end{bmatrix} = \frac{1}{\sqrt{2}} \begin{bmatrix} \zeta_{S_y^A} + \zeta_{S_y^B} \\ \zeta_{S_y^A} - \zeta_{S_y^B} \\ \zeta_{S_x^A} + \zeta_{S_x^B} \\ \zeta_{S_x^A} - \zeta_{S_x^B} \end{bmatrix}. \quad (56)$$



FIG. 11. Figures of merit with uniform losses (NRPD) for $\bar{N} = 0.05 - 0.3$ ($\Delta N = 0.05$). Figures 11(a) and 11(b) show the F_1 fidelities for varying pre-transmission and photodetection efficiencies, respectively, with all other efficiencies fixed at $\eta = 0.9$. Fig. 11(c) shows heralding probability for varying pre-transmission efficiency.

Rewriting Eqn. 55 in terms of ζ , the characteristic function is now

$$\begin{aligned}
 \chi_A^{\rho_{\text{out}}}(\zeta) &= e^{-(1+\eta_m \bar{N}) \left(|\zeta_{S_y^A}|^2 + |\zeta_{S_x^A}|^2 + |\zeta_{S_y^B}|^2 + |\zeta_{S_x^B}|^2 \right)} \\
 &\cdot e^{-(1+\bar{N}) \left(|\zeta_{I_y^A}|^2 + |\zeta_{I_x^A}|^2 + |\zeta_{I_y^B}|^2 + |\zeta_{I_x^B}|^2 \right)} \\
 &\cdot e^{\tilde{N} \sqrt{2\eta_m} \left[\text{Re}(\zeta_{S_x^A} \zeta_{I_y^A}) + \text{Re}(\zeta_{S_x^B} \zeta_{I_y^A}) - \text{Re}(\zeta_{S_y^A} \zeta_{I_x^A}) \right]} \\
 &\cdot e^{\tilde{N} \sqrt{2\eta_m} \left[\text{Re}(\zeta_{S_x^A} \zeta_{I_y^B}) - \text{Re}(\zeta_{S_x^B} \zeta_{I_y^B}) - \text{Re}(\zeta_{S_y^A} \zeta_{I_x^B}) \right]} \\
 &\cdot e^{\tilde{N} \sqrt{2\eta_m} \left[\text{Re}(\zeta_{S_y^B} \zeta_{I_x^B}) - \text{Re}(\zeta_{S_y^B} \zeta_{I_x^A}) \right]} \quad (57)
 \end{aligned}$$

A useful property of Gaussian antinormally-ordered characteristic functions is that they can be renormalized into a probability density function, whose moments can be calculated. We find the heralding probability and fi-

delity by re-expressing Eqn. 57 as

$$\chi_A^{\rho_{\text{out}}}(\zeta) = \frac{\pi^8 p_{\mathbf{Z}}(\zeta)}{D_1} \quad (58)$$

where $p_{\mathbf{Z}}(\zeta)$ is the probability density function for a zero-mean Gaussian random vector ζ with covariance matrices

$$\begin{aligned}
 \langle \zeta \zeta^\dagger \rangle &= \frac{1}{D_1} \begin{bmatrix} (1 + \eta_m \bar{N}) \mathbf{I}_{4 \times 4} & \mathbf{0}_{4 \times 4} \\ \mathbf{0}_{4 \times 4} & (1 + \bar{N}) \mathbf{I}_{4 \times 4} \end{bmatrix} \\
 \langle \zeta \zeta^T \rangle &= \frac{1}{D_1} \begin{bmatrix} \mathbf{0}_{4 \times 4} & \mathbf{N}_{4 \times 4} \\ \mathbf{N}_{4 \times 4}^T & \mathbf{0}_{4 \times 4} \end{bmatrix} \quad (59)
 \end{aligned}$$

for

$$\mathbf{N}_{4 \times 4} = \tilde{N} \sqrt{2\eta_m} \begin{bmatrix} 0 & 0 & -1 & -1 \\ 0 & 0 & -1 & 1 \\ 1 & 1 & 0 & 0 \\ 1 & -1 & 0 & 0 \end{bmatrix} \quad (60)$$

and determinant $D_1 = (1 + \eta_m \bar{N})^4 (1 + \bar{N})^4 - 256 \tilde{N}^8 \eta_m^4$. The output density operator of the Stokes field can be

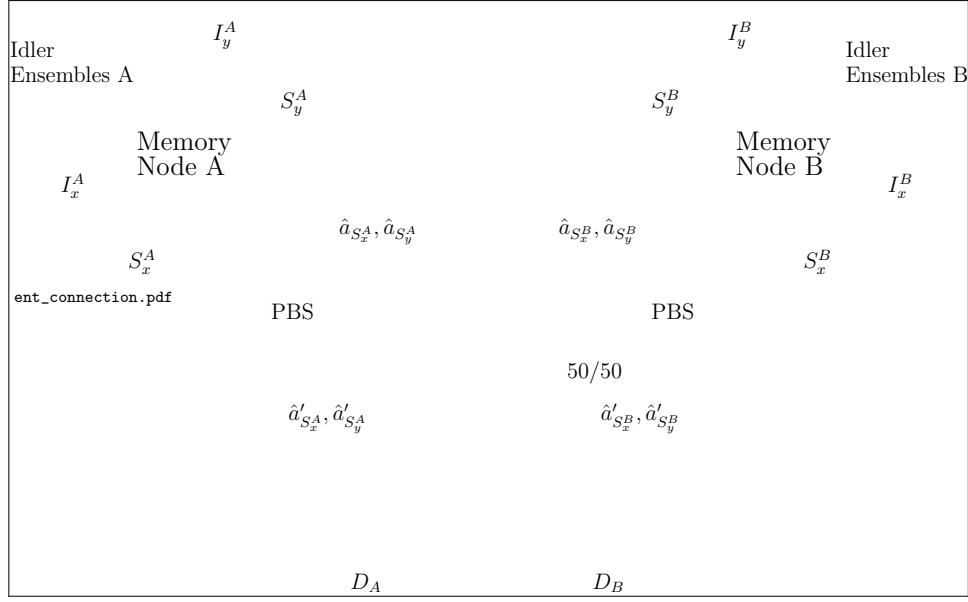


FIG. 12. Polarization entanglement connection. We assume that ensembles A and B are independently in polarization singlet states or Gaussian states following entanglement distribution in Section II.1. The anti-Stokes photons from reading the A and B signal ensembles are interfered at the 50/50 beam splitter. Photon detections at D_A and D_B heralds entanglement connection between the idler ensembles A and B.

expressed as the operator-valued Fourier transformation of Eqn. 57:

$$\begin{aligned} \hat{\rho}_{\text{out}} = & \int \prod_{i=x,y} \frac{d^2 \zeta_{I_i^A}}{\pi^2} \frac{d^2 \zeta_{I_i^B}}{\pi^2} D_N \left(\hat{S}_{I_i^A}, \zeta_{I_i^A} \right) D_N \left(\hat{S}_{I_i^B}, \zeta_{I_i^B} \right) \\ & \cdot \int \prod_{i=x,y} \frac{d^2 \zeta_{S_i^A}}{\pi^2} \frac{d^2 \zeta_{S_i^B}}{\pi^2} \chi_A^{\rho_{\text{out}}}(\zeta) \\ & \cdot D_N \left(\hat{a}'_{S_i^A}, \zeta_{S_i^A} \right) D_N \left(\hat{a}'_{S_i^B}, \zeta_{S_i^B} \right), \end{aligned} \quad (61)$$

where $D_N(\hat{a}_i, \zeta_i) = e^{-\zeta_i \hat{a}_i^\dagger} e^{\zeta_i^* \hat{a}_i}$ is the normally-ordered displacement operator. To perform trace operations on the operator-valued Fourier transform in Eqn. 61, we know that

$$\langle 0 | D_N(\hat{a}_i, \zeta_i) | 0 \rangle = 1 \quad \langle 1 | D_N(\hat{a}_i, \zeta_i) | 1 \rangle = 1 - |\zeta_i|^2 \quad (62)$$

and that

$$\begin{aligned} \text{tr} [D_N(\hat{a}_i, \zeta_i)] &= \pi \delta(\zeta_i) \\ \text{tr} \left[D_N(\hat{a}_i, \zeta_i) \left(\hat{I} - |0\rangle\langle 0| \right) \right] &= \pi \delta(\zeta_i) - 1. \end{aligned} \quad (63)$$

Performing trace operations on the \hat{a}_i mode of an output density operator is equivalent to setting $\zeta_i = 0$ in its characteristic function, so any Gaussian moment calculations in the following may involve a marginal distribution of that specified by Eqn. 59.

We will first consider the particular case of a \mathbf{y} -polarized click at D_A and a \mathbf{x} -polarized click at D_B , and then extrapolate to other possibilities: a \mathbf{x} -polarized click at D_A and a \mathbf{y} -polarized click at D_B ,

and co-polarized clicks at both D_A and D_B . Applying these trace identities in a PNRD scheme, the post-measurement state of the ensembles is

$$\begin{aligned} \hat{\rho}_{\text{post}}^{yx} = & \frac{1}{P_h^{yx}} \int \prod_{i=x,y} \frac{d^2 \zeta_{I_i^A}}{\pi^2} \frac{d^2 \zeta_{I_i^B}}{\pi^2} D_N \left(\hat{S}_{I_i^A}, \zeta_{I_i^A} \right) D_N \left(\hat{S}_{I_i^B}, \zeta_{I_i^B} \right) \\ & \cdot \int \frac{d^2 \zeta_{S_y^A}}{\pi^2} \frac{d^2 \zeta_{S_x^B}}{\pi^2} \chi_A^{\rho_{\text{out}}}(\zeta) \left(1 - |\zeta_{S_y^A}|^2 \right) \left(1 - |\zeta_{S_x^B}|^2 \right), \end{aligned} \quad (64)$$

where the heralding probability is

$$\begin{aligned} P_h^{yx} = & \int \frac{d^2 \zeta_{S_y^A}}{\pi^2} \frac{d^2 \zeta_{S_x^B}}{\pi^2} \chi_A^{\rho_{\text{out}}} \left(\left[\zeta_{S_y^A}, \zeta_{S_y^B}, \zeta_{S_x^A}, \zeta_{S_x^B}, 0, 0, 0, 0 \right]^T \right) \\ & \cdot \left(1 - |\zeta_{S_y^A}|^2 \right) \left(1 - |\zeta_{S_x^B}|^2 \right). \end{aligned} \quad (65)$$

Applying the Gaussian moment factoring theorem, this heralding probability is

$$\begin{aligned} P_h^{yx} = & \frac{1}{D_2} \langle \left(1 - |\zeta_{S_y^A}|^2 \right) \left(1 - |\zeta_{S_x^B}|^2 \right) \rangle \\ = & \frac{1}{D_2^3} \left[D_2^2 - 2 \left(1 + \eta_m \bar{N} \right) D_2 + \left(1 + \eta_m \bar{N} \right)^2 \right] \\ = & \frac{\eta_m^2 \bar{N}^2 (\eta_m \bar{N} (\eta_m \bar{N} + 3) + 3)^2}{(\eta_m \bar{N} + 1)^{10}}, \end{aligned} \quad (66)$$

where $\langle \rangle$ denotes ensemble averaging treating ζ as a complex-valued Gaussian random vector whose probability density function is a marginal distribution of Eqn. 59,



FIG. 13. Figures of merit for Gaussian state entanglement connection (PNRD and NRPD) for $\bar{N} = 0.01 - 0.05$ ($\Delta N = 0.01$).

with $D_2 = (1 + \eta_m \bar{N})^4$. Note that the second-moments of the signal modes reaching the photodetectors are all identical, so the heralding probabilities for each of the four heralding probabilities mentioned earlier are equal. Therefore, $P_h = 4P_h^{yx}$ for the PNRD case. Applying the trace identities in Eqn 63, the post-measurement joint density operator for the NRPD scheme is

$$\begin{aligned}
 \hat{\rho}_{\text{post}}^{yx} &= \frac{1}{P_h^{yx}} \int \prod_{i=x,y} \frac{d^2 \zeta_{I_i^A}}{\pi^2} \frac{d^2 \zeta_{I_i^B}}{\pi^2} D_N \left(\hat{S}_{I_i^A}, \zeta_{I_i^A} \right) D_N \left(\hat{S}_{I_i^B}, \zeta_{I_i^B} \right) \\
 &\quad \cdot \int \frac{d^2 \zeta_{S_y^A}}{\pi^2} \frac{d^2 \zeta_{S_x^B}}{\pi^2} \chi_A^{\rho_{\text{out}}}(\zeta) \\
 &\quad \cdot \left[\pi \delta \left(\zeta_{S_y^A} \right) - 1 \right] \left[\pi \delta \left(\zeta_{S_x^B} \right) - 1 \right]. \quad (67)
 \end{aligned}$$

Tracing out the idler excitation modes, the NRPD

heralding probability is

$$\begin{aligned}
 P_h^{yx} &= \int \prod_{i=x,y} \frac{d^2 \zeta_{S_i^A}}{\pi^2} \frac{d^2 \zeta_{S_i^B}}{\pi^2} \\
 &\quad \cdot \chi_A^{\rho_{\text{out}}} \left(\left[\zeta_{S_y^A}, \zeta_{S_y^B}, \zeta_{S_x^A}, \zeta_{S_x^B}, 0, 0, 0, 0 \right]^T \right) \\
 &\quad \cdot \left[\pi \delta \left(\zeta_{S_y^A} \right) - 1 \right] \left[\pi \delta \left(\zeta_{S_x^B} \right) - 1 \right], \quad (68)
 \end{aligned}$$

which yields

$$P_h^{yx} = \frac{\eta_m^2 \bar{N}^2}{(\eta_m \bar{N} + 1)^4}. \quad (69)$$

This PNRD heralding probability and PNRD fidelity, as well as the NRPD heralding probability and fidelity are shown in Fig. 13. The results for heralding probability are consistent with our understanding of multiple-excitation effects, as described previously in the context of entanglement distribution in Section II.5: reading from ensembles with a higher average spin excitation \bar{N} will yield more anti-Stokes photons, resulting in a higher likelihood of a heralding event when the photodetectors cannot resolve photon number.

The fidelity, when a y -polarized D_A click and a x -polarized D_B click provide the herald, is given by

$$\begin{aligned}
F_{yx} &= \langle \psi_1 | \hat{\rho}_{\text{post}}^{yx} | \psi_1 \rangle \\
&= \frac{1}{P_h^{yx}} \int \prod_{i=x,y} \frac{d^2 \zeta_{I_i^A}}{\pi^2} \frac{d^2 \zeta_{I_i^B}}{\pi^2} \left[1 - \frac{|\zeta_{I_x^A} \zeta_{I_y^B} - \zeta_{I_y^A} \zeta_{I_x^B}|^2}{2} \right] \\
&\quad \cdot \int \frac{d^2 \zeta_{S_y^A}}{\pi^2} \frac{d^2 \zeta_{S_x^B}}{\pi^2} \chi_A^{\rho_{\text{out}}}(\zeta) \left(1 - |\zeta_{S_y^A}|^2 \right) \left(1 - |\zeta_{S_x^B}|^2 \right) \\
&= \frac{1}{D_1 P_h^{yx}} \langle \left(1 - |\zeta_{S_y^A}|^2 \right) \left(1 - |\zeta_{S_x^B}|^2 \right) \\
&\quad \cdot \left(1 - \frac{|\zeta_{I_x^A} \zeta_{I_y^B} - \zeta_{I_y^A} \zeta_{I_x^B}|^2}{2} \right) \rangle. \tag{70}
\end{aligned}$$

Applying the covariance matrix in Eqn. 59 and the Gaussian moment factoring theorem to these higher-order moment expressions, the PNRD fidelity is given by

$$\begin{aligned}
F_{yx} &= \left[\frac{1}{D_1^3} \left[D_1^2 - 2(1 + \eta_m \bar{N}) 1_2 + (1 + \eta_m \bar{N})^2 \right] \right. \\
&\quad - \frac{1}{2D_1} \left(\frac{2(1 + \bar{N})^2}{D_1^2} - \frac{4(1 + \eta_m \bar{N})(1 + \bar{N})^2 + 8\eta_m \bar{N}^2}{D_1^3} \right) \\
&\quad \left. + \frac{2(1 + \eta_m \bar{N})^2(1 + \bar{N})^2 + 8\eta_m \bar{N}^2(1 + \eta_m \bar{N})(1 + \bar{N})}{D_1^4} \right] \langle \psi_1 | \hat{\rho}_{\text{post}}^{yx} | \psi_1 \rangle \\
&= \frac{1}{P_h^{yx}} \int \prod_{i=x,y} \frac{d^2 \zeta_{I_i^A}}{\pi^2} \frac{d^2 \zeta_{I_i^B}}{\pi^2} \left[1 - \frac{|\zeta_{I_x^A} \zeta_{I_y^B} - \zeta_{I_y^A} \zeta_{I_x^B}|^2}{2} \right] \\
&\quad \cdot \int \frac{d^2 \zeta_{S_y^A}}{\pi^2} \frac{d^2 \zeta_{S_x^B}}{\pi^2} \chi_A^{\rho_{\text{out}}}(\zeta) \left[\pi \delta(\zeta_{S_y^A}) - 1 \right] \left[\pi \delta(\zeta_{S_x^B}) - 1 \right]. \tag{71}
\end{aligned}$$

The F_{xy} fidelity is easily seen to be the same as the F_{yx} fidelity, as in the heralding probability calculation presented earlier. While the F_{xx} and F_{yy} fidelities will also equal, they will differ from the cross-polarized fidelities. To find F_{yy} , we need to evaluate

$$\begin{aligned}
F_{yy} &= \frac{1}{D_1 P_h^{yy}} \langle \left(1 - |\zeta_{S_y^A}|^2 \right) \left(1 - |\zeta_{S_y^B}|^2 \right) \\
&\quad \cdot \left(1 - \frac{|\zeta_{I_x^A} \zeta_{I_y^B} - \zeta_{I_y^A} \zeta_{I_x^B}|^2}{2} \right) \rangle. \tag{72}
\end{aligned}$$

The calculation is identical to that for F_{yx} save for the eighth-order moment.

Comparing Eqn. ?? and ??, it immediately becomes obvious that the F_{yy} and F_{yx} differ in their contribution to the overall entanglement fidelity. Prior to our Gaussian state analysis, we assumed that ensembles A and B had loaded pure singlet states prior to entanglement swapping. Their pure singlet states yield a perfect fidelity in both NRPD and PNRD photodetection schemes with the heralding of cross-polarized photons at detectors D_A and D_B . However, the measurement of co-polarized photons is indistinguishable from a cross-polarized photon measurement, even though entanglement need not be successfully swapped when the herald comes from co-polarized photons. As such, we define the fidelity of entanglement as

$$F_E = \frac{P_s}{P_h} = \frac{2P_h^{yx} F_{yx} + 2P_h^{yy} F_{yy}}{P_h}. \tag{73}$$

Figs. 13(b) and 13(c) show the fidelity of entanglement following a swapping operation. As in polarization entanglement distribution, reading and producing multiple-excitations increases heralding probability at the expense of the entanglement fidelity. In this regard, the fidelity plots for emphasize some significant differences between the PNRD and NRPD cases. From the post-measurement density operator, this NRPD fidelity is given by

$$\begin{aligned}
&= \langle \psi_1 | \hat{\rho}_{\text{post}}^{yx} | \psi_1 \rangle \\
&= \frac{1}{P_h^{yx}} \int \prod_{i=x,y} \frac{d^2 \zeta_{I_i^A}}{\pi^2} \frac{d^2 \zeta_{I_i^B}}{\pi^2} \left[1 - \frac{|\zeta_{I_x^A} \zeta_{I_y^B} - \zeta_{I_y^A} \zeta_{I_x^B}|^2}{2} \right] \\
&\quad \cdot \int \frac{d^2 \zeta_{S_y^A}}{\pi^2} \frac{d^2 \zeta_{S_x^B}}{\pi^2} \chi_A^{\rho_{\text{out}}}(\zeta) \left[\pi \delta(\zeta_{S_y^A}) - 1 \right] \left[\pi \delta(\zeta_{S_x^B}) - 1 \right]. \tag{74}
\end{aligned}$$

Unlike the difference in moment factoring present in the PNRD fidelity calculation, the NRPD fidelity is identical for to cross-polarized and co-polarized photodetection events, as is evident from the NRPD POVM applied in Eqn. 74. This calculation is only dependent on the second-moments of the idler ensembles and the normalizations inherent in the marginal probability distributions following photodetection, each of which is independent of photon polarization. Equation 74 thus simplifies to

$$F_{yx} = \frac{1}{P_h^{yx}} \left[\frac{(\bar{N} + 1)^6 (\eta_m \bar{N} + 1)^7 - 2(\bar{N} + 1)^6 (\eta_m \bar{N} + 1)^6 + 1}{(\bar{N} + 1)^{10} (\eta_m \bar{N} + 1)^9} + \frac{1}{D_1} - \frac{(\bar{N} + 1)^2}{D_1^3} \right], \tag{75}$$

which is plotted in Fig. 13(b). The PNRD case lets us actively discard garbage photodetection events that might result from multiple-excitations present at entanglement distribution. In this case, we know that having match-

ing, *single* counts at D_A and D_B will very likely correspond to a successful entanglement swapping operation with photon-number resolving detectors. On the other hand, high \bar{N} , even in the presence of high measure-

ment efficiency, severely affects our NRPD entanglement fidelity, because NRPD cannot distinguish false heralding events. Also surprising is the ratio of the fidelity of entanglement for cross-polarized and co-polarized photodetection events, as shown in Fig. 13(c). These fidelities are very close to each other, although they begin to diverge as \bar{N} increases. That they are so close in value is somewhat surprising because cross-polarized photodetection was predicted for unity entanglement fidelity in the case of a pure singlet distribution, whereas co-polarized photodetection would not necessarily be indicative of a singlet state remaining in the idler ensembles.

IV. SUMMARY AND OUTLOOK

Two areas in this paper are particularly ripe for extension and exploration: further investigation into the mechanisms and imperfections of ensemble memories that distribute polarization entanglement, and formalizing the number state analysis of systems with loss-modeling beam splitters. Several possible extensions are relatively straightforward, such as the inclusion of phase offsets between orthogonally-polarized paths in during entanglement distribution. Others require a more careful consideration of the underlying physics of quantum memories. For example, the performance analysis of polarization entanglement distribution presented here omits the presence of spin decoherence in the atomic ensembles. In quantifying the singlet-storage fidelity, there is a tradeoff between the time scale of decoherence of Dicke excitations, the time it takes for a single heralding photon to reach a photodetector, and the post-memory transmission efficiency (which scales with the post-transmission length). Spin decoherence of the ensemble may therefore be a significant factor limiting the optimal physical distance that local entanglement distribution can cover. Another possible departure would be to discard the DLCZ approach entirely, using a stimulated Raman or EIT approach, instead of a spontaneous Raman process. The Hamiltonian in this approach would be amenable to a traditional Gaussian state analysis, and would allow for deterministic control of read and write processes in entanglement distribution. As of this writing, however, there is currently no accepted means of nondestructive verification of successful entanglement distribution in a coherently-controlled Λ -level atomic ensemble. This open problem makes certain long-distance quantum communication tasks, such as repeated entanglement connection, difficult to accomplish using a driven Raman process.

Unrelated to the question of memories is formalizing the architectural analysis of loss-modeling beam splitters. The SU(2) number-state representation for *single* beam splitters is discussed in great detail by [23]. Summation compositions of beam splitter coefficients determined important architectural figures of merit—heralding probability, fidelity, and success probability—in the course of this work, but were calculated numerically. With

a number-state basis, what general properties or figures of merit of a quantum network can we determine if we limit ourselves to linear optical elements (e.g., 50-50 and polarizing beam splitters, loss elements), photodetectors, and photon-number conserving nonlinear optical elements (e.g., heralding quantum memories or Kerr crystals)? In particular, do any of the properties of a beam splitter coefficient introduced in Section II permit any useful, analytical simplifications when using the joint density operator of a network to calculate a figure of merit? Is a number-state analysis consistent with a SPDC Gaussian state analysis when nonlinear elements are excluded and we are limited entirely to the propagation of optical fields? Answers to these questions could possibly alleviate the exhausting notational and computational difficulties currently necessitated by number-state analysis.

IV.1. Engineering Quantized Field Absorption

We can compensate for finite detunings and heralding probabilities in these ensembles by increasing the ensemble's optical depth, which is limited in free-space interactions by ensemble size and coupling strength. Several approaches use multi-pass optical cavities to increase the likelihood of a successful Raman scattering event between a cavity field and the enclosed ensemble [7, 11–14]. The cavity-ensemble heralding efficiency is captured by the cooperativity parameter $C = g_c^2 N_A / \kappa_c \gamma$, where g_c is the single-atom coupling constant to the cavity mode, κ_c is the cavity decay rate, and γ is the excited state spontaneous decay rate. It can be shown that the cooperativity is approximately $C \sim f d$, where d is the optical depth of the ensemble and the finesse f is approximately the number of passes the optical field makes in the cavity. Optical cavities are used in the magnon-type memory (Fig. ??), in which a single collective excitation is shared between two spatially-overlapping atomic ensembles [6]. Photons of arbitrary polarization states are stored between two ensembles that absorb only left- (σ^+) and right-circularly (σ^-) polarized light, respectively, and emit only linearly (π) polarized light into the cavity resonator, thereby eliminating any which-path information. The memory itself is an ensemble of approximately 8000 cesium atoms loaded from a far-detuned magneto optical trap (MOT) into a one-dimensional optical lattice overlapping a medium-finesse ($f = 140$) optical cavity. A spatially homogenous, DC magnetic field allows time-dependent control of polarization storage through Larmor precession of the ensembles magnetic moment. In theory, single-photon conversion efficiencies for this type of magnon memory are quite high. It was also shown in Section ?? and Appendix ?? that a heralding quantum memory operating with a single- or few-photon pump field performs a ‘non-Gaussian’ operation because of its Hamiltonian’s (Eqn. 7) algebraic symmetries. Several approaches exist for enhancing nonlinear optical effects be-

tween optical and ensemble excitations, such as optically imprinted Bragg mirrors ([26, 27]), interactions between ensembles of atoms in optical lattices ([28]), and atomic blockades using Rydberg-level atoms ([29]).

Bandwidth requirements for atomic ensembles impose restrictions on the phase matching bandwidth of our polarization-entanglement source. In Section I.2, we introduced OPA sources for polarization entanglement. To be compatible with ensemble-based quantum memories and enable efficient quantum state transfer, the signal and idler output fields must be nearly-resonant with the center frequency of the desired atomic transition and have a narrow spectral bandwidth—anywhere between 10 and 100 MHz—matching that of the ensemble [20].

There are two techniques for reducing the spectral bandwidth of the output from spontaneous parametric down conversion. The first is cavity-enhanced down conversion, in which a nonlinear crystal in a cavity will only emit light in prescribed cavity modes. Because

cavity output is spectrally multimode, a Fabry-Perot etalon or filter cavity is required to select a single cavity mode [30, 31]. Recently, groups have created type-II polarization entanglement sources compatible with alkali-gas ensembles of rubidium and cesium by applying spectral filtering and frequency locking, resulting in bandwidths of 2.7 MHz and 9.6 MHz, and corresponding spectral brightnesses of approximately 330 and 6 entangled pairs per second per mW of pump power per MHz of output bandwidth [32, 33].

ACKNOWLEDGMENTS

We thank F. Wong, V. Vuletić, Z. Dutton, S. Johnson, M. Tobenkin, R. Nair, and B. J. Yen for useful discussions and advice. This work was supported by the DARPA Quantum Entanglement Science and Technology (QuEST) program.

-
- [1] H. J. Kimble, *Nature* **453**, 1023 (2008).
 - [2] S. Lloyd, M. S. Shahriar, J. H. Shapiro, and P. R. Hemmer, *Phys. Rev. Lett.* **87**, 167903 (2001).
 - [3] J. H. Shapiro and N. C. Wong, *Journal of Optics B: Quantum and Semiclassical Optics* **2**, L1 (2000).
 - [4] L.-M. Duan, M. D. Lukin, J. I. Cirac, and P. Zoller, *Nature* **414**, 413 (2001).
 - [5] R. H. Dicke, *Phys. Rev.* **93**, 99 (1954).
 - [6] H. Tanji, S. Ghosh, J. Simon, B. Bloom, and V. Vuletić, *Phys. Rev. Lett.* **103**, 043601 (2009).
 - [7] J. Simon, H. Tanji, J. K. Thompson, and V. Vuletić, *Phys. Rev. Lett.* **98**, 183601 (2007).
 - [8] S. M. Barnett and P. M. Radmore, *Methods in Theoretical Quantum Optics* (Oxford Science Publications, 1997).
 - [9] A. B. Klimov and S. M. Chumakov, *A Group-Theoretical Approach to Quantum Optics: Models of Atom-Field Interactions* (Wiley, 2009).
 - [10] S. L. Braunstein and P. van Loock, *Rev. Mod. Phys.* **77**, 513 (2005).
 - [11] V. Josse, A. Dantan, A. Bramati, M. Pinard, and E. Giacobino, *Phys. Rev. Lett.* **92**, 123601 (2004).
 - [12] A. T. Black, J. K. Thompson, and V. Vuletić, *Phys. Rev. Lett.* **95**, 133601 (2005).
 - [13] C. Simon, H. de Riedmatten, M. Afzelius, N. Sangouard, H. Zbinden, and N. Gisin, *Phys. Rev. Lett.* **98**, 190503 (2007).
 - [14] J. K. Thompson, J. Simon, H. Loh, and V. Vuletić, *Science* **313**, 74 (2006), <http://www.sciencemag.org/content/313/5783/74.full.pdf>.
 - [15] M. Fleischhauer and M. D. Lukin, *Phys. Rev. A* **65**, 022314 (2002).
 - [16] M. D. Lukin, *Rev. Mod. Phys.* **75**, 457 (2003).
 - [17] A. V. Gorshkov, A. André, M. Fleischhauer, A. S. Sørensen, and M. D. Lukin, *Phys. Rev. Lett.* **98**, 123601 (2007).
 - [18] A. V. Gorshkov, A. André, M. D. Lukin, and A. S. Sørensen, *Phys. Rev. A* **76**, 033804 (2007).
 - [19] J. H. Shapiro, *New Journal of Physics* **4**, 47 (2002).
 - [20] N. Sangouard, C. Simon, H. de Riedmatten, and N. Gisin, *ArXiv e-prints* 0906.2699 (2009), [arXiv:0906.2699 \[quant-ph\]](https://arxiv.org/abs/0906.2699).
 - [21] W. K. Wootters and W. H. Zurek, *Nature* **299**, 802 (1982).
 - [22] O. Thomas, Z. L. Yuan, J. F. Dynes, A. W. Sharpe, and A. J. Shields, *Applied Physics Letters* **97** (2010), cited By (since 1996) 1.
 - [23] R. A. Campos, B. E. Saleh, and M. C. Teich, *Phys. Rev. A* **40**, 1371 (1989).
 - [24] M. Razavi and J. H. Shapiro, *Phys. Rev. A* **73**, 042303 (2006).
 - [25] N. Lütkenhaus, J. Calsamiglia, and K.-A. Suominen, *Phys. Rev. A* **59**, 3295 (1999).
 - [26] A. André and M. D. Lukin, *Phys. Rev. Lett.* **89**, 143602 (2002).
 - [27] M. Bajcsy, A. S. Zibrov, and M. D. Lukin, *Nature* **426**, 638 (2003).
 - [28] C. A. Muschik, I. de Vega, D. Porras, and J. I. Cirac, *Phys. Rev. Lett.* **100**, 063601 (2008).
 - [29] M. D. Lukin, M. Fleischhauer, R. Cote, L. M. Duan, D. Jaksch, J. I. Cirac, and P. Zoller, *Phys. Rev. Lett.* **87**, 037901 (2001).
 - [30] C. E. Kuklewicz, F. N. C. Wong, and J. H. Shapiro, *Phys. Rev. Lett.* **97**, 223601 (2006).
 - [31] M. Scholz, L. Koch, and O. Benson, *Phys. Rev. Lett.* **102**, 063603 (2009).
 - [32] M. Scholz, L. Koch, R. Ullmann, and O. Benson, *Applied Physics Letters* **94**, 201105 (2009).
 - [33] X.-H. Bao, Y. Qian, J. Yang, H. Zhang, Z.-B. Chen, T. Yang, and J.-W. Pan, *Phys. Rev. Lett.* **101**, 190501 (2008).